Reconstructing the Mesozoic evolution of the Gulf of Mexico Basin: A new model incorporating optimised and focused lithospheric deformation

Satyam Pratap Singh[1], Sabin Zahirovic[1], Maria Seton[1], Nicky M. Wright[1], Nicholas Atwood[2], Catherine Belgarde[2], Claire Mallard[1]

[1]EarthByte Group, School of Geosciences, The University of Sydney, NSW 2006, Australia

[2]BHP Metals Exploration, Tucson, Arizona 85704, USA

Corresponding author: Satyam Pratap Singh (satyampratap.singh@sydney.edu.au)

Key Points:

- A optimised deformable plate model for Gulf of Mexico (GoM) is introduced that dynamically adjusts stretching factor during rift evolution.
- The 40 Myrs gap in GoM's Mesozoic strata is due to rapid subsidence, shifting red bed deposition beneath Jurassic salt formations.
- The GoM basin transitioned from a magma-rich to a hyperextended margin with possible mantle exhumation.

Abstract

The Gulf of Mexico (GoM) is one of the most extensively studied offshore regions, but its Mesozoic evolution remains uncertain. The presence of a thick sedimentary cover and Jurassic salt poses challenges for geophysical imaging, hindering our understanding of the Mesozoic depositional history and crustal architecture evolution. Current tectonic models with rigid plates fail to capture key aspects of GoM evolution. This study introduces a new deformable plate model with optimised focused deformation designed to dynamically adjust stretching factors (SF) during rift evolution. Our model, which calculates crustal thickness and tectonic subsidence (TS) through time and accounts for stretching and thermal subsidence, can explain the depositional history of the pre-salt section and crustal architecture evolution of the GoM. Our model produces a predicted present-day crustal thickness with a root mean square error of 5.6 km with the GEMMA crustal thickness model. The resultant TS of ~1.5 km before the Yucatán block drifted, provides routes for the deposition of red beds through the paleo drainage systems of the northern GoM as successor basin infilling. The model explains ~40 Myrs of missing sedimentary strata, which we attribute to rapid subsidence in the central GoM, shifting red beds deposition beneath the Jurassic salt formations. Extension rate and SF calculations reveal a transition from a magma-rich to a hyperextended margin, with possible mantle exhumation. Our model can be useful in understanding the extent of other Jurassic deposits in the GoM basin and offers a robust framework for comprehending global passive rift margin evolution.

Plain Language Summary

Unveiling the Gulf of Mexico's (GoM) hidden Mesozoic history has been challenging due to its thick sedimentary cover and Jurassic salt deposits. Existing models using rigid plates have fallen short in explaining the GoM's evolution. In this study, we introduce a new approach - a deformable plate model that dynamically adjusts for stretching factors during rift evolution. Our model successfully explains the pre-salt sedimentary history and crustal architecture evolution of the GoM. It predicts current crustal thickness with impressive accuracy. Our findings suggest that before the Yucatán block shifted, about 1.5 km of tectonic subsidence occurred, allowing for the deposition of red beds in the northern GoM. Our model also solves a mystery - the absence of around 40 million years of sedimentary layers - by proposing rapid subsidence in the central GoM, shifting red bed deposition beneath Jurassic salt formations. Calculations reveal a transition from a magma-rich to a hyperextended margin, with potential mantle exhumation. Importantly, our model provides a valuable tool for understanding Jurassic deposits in the GoM and offers insights into global rift margin evolution.

1 Introduction

The Gulf of Mexico (GoM) is shrouded in thick sedimentary layers, which conceal its oldest rocks and makes it challenging to trace its Mesozoic geological evolution (Filina et al., 2022). While seismic reflection data provides a means of seeing through the cover, the availability of these datasets for the region is limited, as much of it is proprietary. Furthermore, the complex interplay between thick sedimentary layers and pervasive mobile salts makes it difficult to conduct detailed seismic imaging and investigate the pre-salt structures (Christeson et al., 2014; Eddy et al., 2014), further obscuring its Mesozoic tectonic history.

Based on the available geophysical and geological constraints, numerous tectonic models have been proposed for the formation of the GoM. Although these models generally agree on the broader framework for the GoM formation, including the initiation of rifting after the Ouachita-Marathon orogeny (which formed from the collision of Laurentia with Gondwana) in the Late Paleozoic era and the completion of seafloor spreading by the mid Early Cretaceous period, they vary in several aspects (Escalona et al., 2021; Marton & Buffler, 1994; Minguez et al., 2020; Pindell et al., 2021; Pindell & Kennan, 2009). These key differences include the interpretation of Triassic red bed deposition, the timing of initiation of continental rifting, timing of salt deposition in relation to oceanic crust formation, the mode of the breakup, and the pre-rift GoM fit of the crustal blocks. For example, the conventional model for red bed formation suggests that red bed deposition occurred in rifts and grabens during initial Pangea rifting during the Late Triassic attributed to the existence of the South Georgia Rift (SGR) in eastern North America (Figure 1; Salvador, 1991). However, such rift-graben structure is not pervasively observed in seismic section across the GoM basin suggesting some alternative model for red bed deposition (Filina et al., 2022; Milliken, 1988; Nicholas & Waddell, 1989; J. W. Snedden & Galloway, 2019). Further complicating the understanding of red bed deposition is the several millions of years of hiatus in stratal deposition between the Triassic red beds and the overlying Jurassic Louann salt (Filina et al., 2022; Marton & Buffler, 1994; Salvador, 1991). In a broader sense, there are certain regions along the Yucatán margin and eastern GoM basin (Figure 1 and 2) that exhibit pre-salt deposits, evident in seismic sections (Horn et al., 2016; O'Reilly et al., 2017; Williams-Rojas et al., 2012). However, the precise model for their formation, and whether they represent red bed deposits, remain uncertain due to the challenges posed by the thick sedimentary cover impeding drilling efforts.

Gravity and seismic data indicate a significant portion of the GoM basin has a thinner crust than typical continental crust, necessitating compensation to establish a closer fit between North and South America before the breakup of Pangea (Christeson et al., 2014; Eddy et al., 2014; Filina, 2019). Based on these data, two plausible scenarios are postulated: either hyperextension and mantle exhumation or the formation of thick oceanic crust preceding the primary opening of the GOM during the Late Jurassic-Early Cretaceous (Filina & Beutel, 2022; Lundin & Doré, 2017; Pindell et al., 2021). Moreover, seaward-dipping reflectors (SDRs), commonly associated with magma-rich margins, have been observed in the seismic section of the eastern GoM (Filina et al., 2022). Interestingly, seismic reflection data also reveals the presence of ridge-like basement highs in the central to the northeastern half of the basin and at specific locations along the northern Yucatán margin (Pindell et al., 2014). Notably, such ridge-like features are typically associated with mantle exhumation and often related to magma-poor margins (Minguez et al., 2020; Pindell et al., 2014). Consequently, the nature of rifting in the GoM, whether it leans towards a magma-rich or magma-poor scenario, and the exact architecture of the crust formed during seafloor spreading, including stretched continental crust, thicker oceanic crust, or exhumed mantle, remain enigmatic.

The prevailing plate tectonic models for the opening of the GoM have predominantly employed rigid plate assumptions (Filina & Beutel, 2022; Marton & Buffler, 1994; Minguez et al., 2020; Pindell et al., 2021). However, a significant limitation of these models is their assumption that the continental crust remained intact and undeformed during the opening of the basin, which contradicts compelling geological and geophysical data from passive margins (Eddy et al., 2014,

2018; Minguez et al., 2020; Rowan, 2014; Van Avendonk et al., 2015). In the GoM, seismic reflection and gravity interpretations offer insights into the significant amount of subsidence and deformation of the crust throughout its evolution, posing significant challenges to the rigid plate model (Filina et al., 2022; Pindell et al., 2014). Moreover, the presence of thin, high-velocity layers within the continental crust is believed to be remnants of the original pre-rift crust that experienced thinning and stretching during the opening of the GoM basin (Christeson et al., 2014; Eddy et al., 2014; Filina et al., 2022). These observations can only be adequately explained by adopting a deformable plate model that captures the deformation and evolution of the continental crust.

Here we present a new deformable plate reconstruction model with an optimised focused deformation approach to reconstruct the Mesozoic history of the GoM. The core of our optimised focused deformation model lies in its ability to dynamically adjust the region between rigid blocks, accounting for the extent of thinning experienced during the rifting phase. This adjustment is meticulously tailored to exponentially increase the stretching factors seaward, ultimately leading to continental rupture and the formation of oceanic crust. Through our new approach, we aim to advance the understanding of the GoM's complex Mesozoic geological history, providing a comprehensive framework for interpreting its evolution and the key geological processes that have shaped the region.

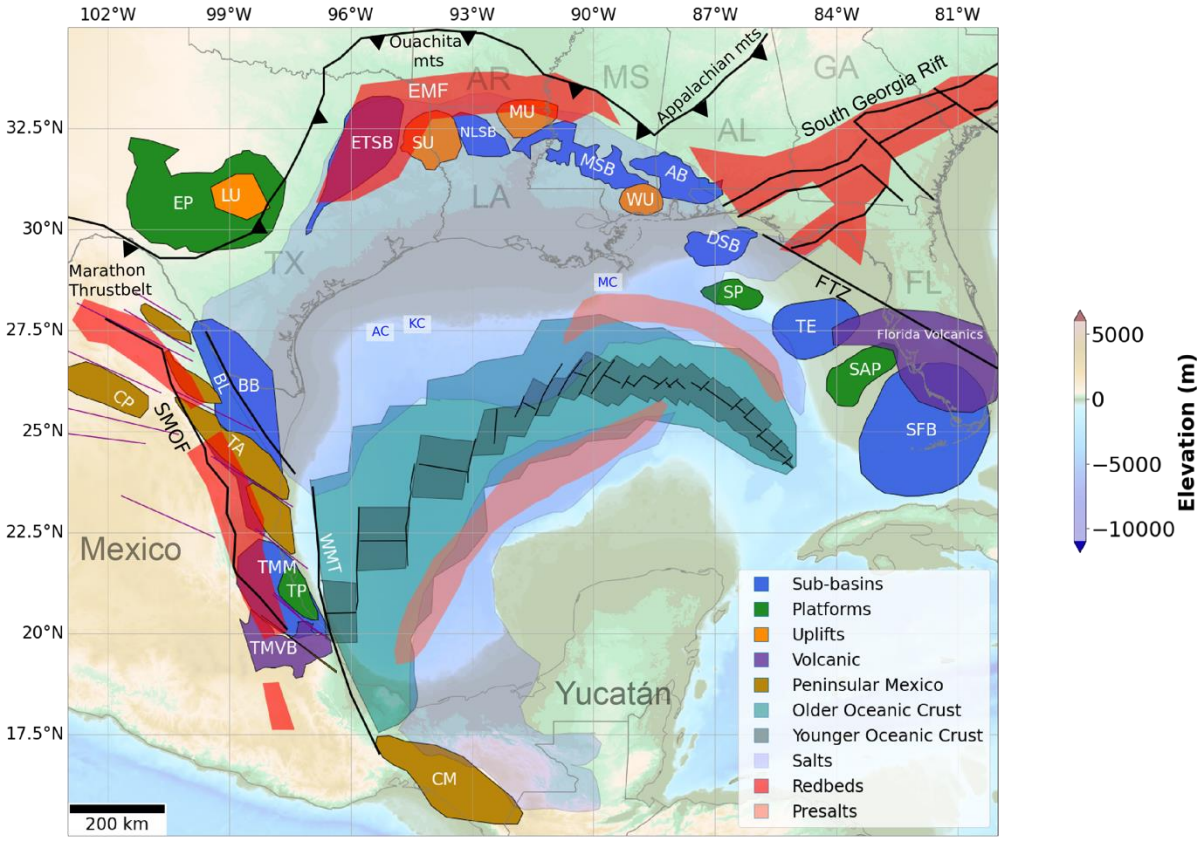

Figure 1. Tectonic elements in the GoM basin. Abbreviations: AB, Alabama basin; AC, Alaminos Canyon; BB, Burgos basin; BL, Burgos lineament; CM, Chiapas Massif; CP, Coahuila Platform; DSB, DeSoto salt basin; EP, Edwards platform; ETSB, East Texas salt basin; EMF, Eagle Mills Formation; FTZ, Florida Transfer Zone; KC, Keathley Canyon; LU, Llano uplift; MC, Mississippi Canyon; MSB, Mississippi basin; MU, Monroe uplift; NLSB, North Louisiana salt basin; SAP, Sarasota platform; SFB, South Florida basin; SMOF, Sierra Madre Oriental Fault; SP, Southern platform; SU, Sabine uplift; TA, Tamaulipas/San Carlos arch; TE, Tampa embayment; TMM, Tampico–Misantla–Magiscatzin; TMVB, Trans-Mexican Volcanic Belt; TP, Tuxpan platform; WU, Wiggins Uplift; WMT, Western Margin Transform. US States are abbreviated as TX, Texas; LA, Louisiana; AR, Arkansas; Ms, Mississippi; Al, Alabama and GA, Georgia. Figure modified after Snedden and Galloway (2019). Purple lines represent an en echelon fault array from Pindell et al. (2021) that influenced the motion of Peninsular Eastern Mexico during GoM rifting. CM and Oceanic Crust data are also from Pindell et al. (2021). The presalt basins are based on Filina et al. (2022).

2 Geological History

2.1 Rifting Initiation and Early Magmatism

During the Late Triassic period, the Yucatán region was connected to the North American plate, with its northern boundary marked by the Ouachita mountains and the western boundary demarcated by the Burgos lineament (BL) (Figure 1; Pindell et al., 2021; Snedden & Galloway, 2019). Continental crustal extension commenced with rift development in eastern North America and back-arc rifting in Mexico (Izquierdo-Llavall et al., 2022; Pindell, 1985; Pindell et al., 2021). The exact timing of rift initiation is harder to constraint given the limited wells located in the northern GoM basin and Mexico. Nevertheless, most model suggests that the rifting started in Late Triassic (Escalona et al., 2021; Izquierdo-Llavall et al., 2022; Lundin & Doré, 2017; Pindell et al., 2021). This rift formation in eastern North America coincided with a period of intense magmatic activity known as the Central Atlantic Magmatic Province (CAMP). Large quantities of lava, dykes, and sills have been mapped, dating around 200 Ma marking a peak in CAMP magmatism (Marzoli et al., 2018). However, it is important to note that the extension between the Yucatán block and North America was relatively minor during this time, indicating a distinct tectonic behaviour compared to the rift development in other areas of the GoM (Kneller & Johnson, 2011; Pindell et al., 2021; Snedden & Galloway, 2019).

2.2 Red bed deposition

After the initiation of rifting and magmatism, the northern and eastmost regions of the GoM, as well as eastern Mexico, witnessed the deposition of distinctive sedimentary units comprising red to greenish-grey shales, white sandstones, and red dolomites, collectively forming the Eagle Mills Formation (Figure 1; Salvador, 1991; Snedden & Galloway, 2019). The age of the Eagle Mills Formation is considered to be Triassic (Carnian; 237–228.4 Ma) based on the discovery of a single-leaf fossil (*Macrotaeniopteris magnifolia*) in the Humble #1 Royston well (Arkansas, USA; Scott et al., 1961). Additional support for its Triassic age stems from fossil algae analysis (Horn et al., 2016; Williams-Rojas et al., 2012). To the west of the GoM basin, the Triassic

section in northeastern Mexico primarily consists of similar red beds, but with a relatively higher proportion of volcanic rocks due to differing tectonic settings (Shann & Horbury, 2020). Nevertheless, the precise dating of these rocks remains uncertain, and they are generally considered Late Triassic to Early Jurassic in age (Cisneros & Lawton, 2011). Notably, these red beds often exhibit interbedding with the CAMP lavas and sills (Frederick et al., 2020).

The significance of these Triassic deposits lies in their representation of the transitional phase between the Paleozoic Ouachita-Marathon orogeny and the subsequent Mesozoic rifting, which ultimately gave rise to the formation of the GoM. Traditionally, the prevailing model (Salvador, 1991) suggests that these red beds were deposited within grabens formed during the early stages of Pangea rifting, primarily attributed to the presence of the Triassic South Georgia Rift (SGR) in eastern North America (Figure 1). However, recent observations and a re-evaluation of older seismic data have cast doubts on this conventional model. Seismic data from Arkansas, Louisiana, and Texas reveal a lack of clear evidence for such extensive buried rift system in the areas where the grabens were expected to be present (Milliken, 1988; Nicholas & Waddell, 1989; Snedden & Galloway, 2019). Although, few basement fault like structures have been observed in some seismic sections of northern GoM margin but they are not pervasive and very limited to northern GoM (Frederick et al., 2020). Additionally, in north Texas, the Eagle Mills Formation onlaps the deformed Paleozoic basement (Milliken, 1988), suggesting sediment infilling rather than deposition in grabens. Moreover, recent seismic images demonstrate that the seismic horizon of the base salt is predominantly unfaulted (Horn et al., 2016). Considering these findings, an alternative model has emerged, proposing that the northern GoM experienced minimal stretching during Late Triassic, and the red beds represent a successor basin deposit resulting from the infilling of pre-existing accommodation created during the Ouachita-Marathon orogeny (Snedden & Galloway, 2019). Moreover, the lithosphere may have thinned in a more ductile manner after this minimal stretching phase (Pindell et al., 2021). This new perspective challenges the traditional understanding of the GoM evolution and warrants further investigation into the origin and depositional processes of the Late Triassic to Early Jurassic red beds.

2.3 Pre-salt sedimentary basins

The U-Pb analyses of well data from the northern GoM reveal that the youngest depositional age of the red beds extended only until 205 Ma, followed by a significant hiatus until the deposition of post-rift salt at 169 Ma (Dickinson et al., 2010; Umbarger, 2018; Wiley, 2017). The cause of this missing stratal gap remains unknown. Intriguingly, multiple seismic surveys conducted in the northern Yucatán margin, western and eastern GoM have identified thick pre-salt sediments, indicating their presence in these regions (Horn et al., 2016; O'Reilly et al., 2017; van Avendonk et al., 2015; Williams-Rojas et al., 2012). However, the western GoM presents challenges in imaging through the extensive overlying salt (Horn et al., 2016; Williams-Rojas et al., 2012), leading to ongoing debates regarding the existence of pre-salt sediments in this area. In the northwestern part of the GoM basin along the GUMBO1 (Gulf of Mexico Basin Opening) seismic profile (Figure 3), van Avendonk et al. (2015) proposed the presence of pre-salt sediments based on P-wave velocities between 5 and 5.5 km/s (Figure 4). Conversely, Filina (2019) offered alternative interpretations, considering potential fields, such as the presence of a very thick salt layer or a "salt wall". Nevertheless, the Yucatán margin has been covered by multiple seismic sections and modelled gravity and magnetic data supporting the existence of pre-salt sedimentary layers, with estimated thicknesses ranging from 2 to 5 km (Figure 2, 4 and

5). Despite these observations, the precise formation processes of these pre-salt sediments remain elusive due to the challenges associated with drilling through thick sedimentary layers.

2.4 Rift-to-Drift transition and crustal extension

The Yucatán block underwent a significant transformation during the Early and Middle Jurassic period (~195 to ~170 Ma) as it transitioned from rift to drift, resulting in substantial stretching and thinning of the continental crust. This process led to the development of a large region of transitional crust (Figure 3, 4, and 5). Numerous models have been proposed to explain the rift-to-drift transition in the GoM (Escalona & Yang, 2013; Filina et al., 2022; Minguez et al., 2020; Pindell et al., 2021). Some suggest clockwise rotation of Yucatán (Freeland & Dietz, 1971), while others propose anticlockwise rotation (Marton & Buffler, 1994; Minguez et al., 2020; Pindell et al., 2021), and some even propose a southeast translation of the Yucatán block (Anderson & Schmidt, 1983). However, with the availability of geophysical data, it is now well understood that the Yucatán block underwent significant anticlockwise rotation. Paleomagnetic data have revealed an approximate 60-degree rotation of the Chiapas Massif and Yucatán block (Marton & Buffler, 1994). Seismic data has mapped fracture zones in the eastern GoM (Christeson et al., 2014; Eddy et al., 2014), while gravity data has identified fracture zones and Extinct Spreading Centres (Minguez et al., 2020). Aeromagnetic data has been used to map seafloor rotational fabrics in the western and central GoM, revealing the presence of anticlockwise rotation. However, precisely quantifying the amount of Yucatán rotation remains challenging (Pindell et al., 2021).

On the easternmost side of the GoM basin (Figure 1), this rift-to-drift transition is associated with various basement features, including the Florida Transfer Zone (FTZ; Marton & Buffler, 1994; Pindell et al., 2021; Pindell & Kennan, 2009). Evidence of increased Mesozoic extension is observed through early Mesozoic volcanism in the area south of the FTZ (Figure 1). However, the distribution of deformation during this transition remains poorly understood (Filina et al., 2022; Pindell et al., 2021).

Crustal thickness estimates from the GUMBO seismic refraction experiment and GEMMA crustal thickness model (Reguzzoni & Sampietro, 2015) reveal contrasting stretching patterns between the eastern and western regions of the GoM (van Avendonk et al., 2015). The central and western GoM region (Figure 3) exhibits distinctive extension characteristics. Unlike typical rifted margins, which are usually less than 300 km wide (Harry et al., 2003), this region displays an unusually broad area of highly extended crust spanning approximately 425 to 500 km in the western and central GoM (Huerta & Harry, 2012). Conversely, the eastern portion of the North American GoM margin is less than 250 km wide (Huerta & Harry, 2012). Moreover, the northern GoM basin is marked by a series of elevated basement blocks associated with thick and less extended continental crust, while deep basins containing thick salt accumulations are interspersed between them, characterised by thinner and more extended continental crust (Marton & Buffler, 1994). One prominent geological feature is the Sabine uplift, believed to have formed as a mid-rift high during the opening of the GoM in the Triassic period (Adams, 2007). Geophysical data confirms the Sabine uplift as a block of thick crust, with deep wells recovering late Paleozoic sediments and Mississippian volcanic rocks (Marton & Buffler, 1994). These Mesozoic uplifted areas experienced subsequent phases of reactivation and further uplift

during the middle to late Cretaceous and Paleocene-Eocene (Adams, 2007). The shape and style of these resulting uplifted areas were strongly influenced by pre-Jurassic northwest-southeast transform fault lineaments. The variations in crustal stretching and the presence of elevated blocks and deep basins in different regions of the GoM highlight the complex and heterogeneous nature of the rift-to-drift transition, shedding light on the intricate processes involved in the evolution of this dynamic basin.

2.5 SDRs and magnetic anomalies formation

Seismic data analysis in the northeastern and southern parts of the GoM basin, along the Yucatán margin, has revealed the presence of basinward-dipping reflections known as SDRs (Eddy et al., 2014; Hudec et al., 2013; Hudec & Norton, 2019; Williams-Rojas et al., 2012). These SDR complexes exhibit significant deformation and are believed to have formed due to intense magmatic activity, probably during the CAMP magmatism event (Filina et al., 2022). Notably, these SDRs align with prominent magnetic anomalies in the region, suggesting a close association with rift-related magmatism (Figure 2). The magnetic anomalies exhibit distinct characteristics, such as long-wavelength, rounded, or oblate shapes. One particularly noteworthy magnetic high running north-south off the western Yucatán shelf margin is referred to as the Campeche magnetic anomaly (CMA). The CMA shares similarities in shape and intensity with the prominent Houston magnetic anomalies (HMA) and Florida magnetic anomalies (FMA) found along the northern continental margin of the GoM (Pindell et al., 2016). Potential field modelling suggests that the CMA are likely associated with volcanic flows formed within the syn-rift sections of rift basins (Pindell et al., 2016). However, due to their significant burial depth, it remains challenging to determine whether they are indeed SDRs. A similar origin has been proposed for the HMA (Mickus et al., 2009). Furthermore, the Yucatán magnetic anomaly (YMA) in the southern GoM basin also coincides with interpreted SDRs observed in seismic images (Filina et al., 2022; Steier & Mann, 2019). The identification of SDRs and their association with magnetic anomalies provides crucial insights into the magmatic processes and tectonic evolution of the GoM. These intriguing findings support the interpretation of the GoM as a magma-rich margin.

2.6. Salt deposition

During the mid-Jurassic, basin-wide salt was deposited in the GoM, but there remains a debate regarding the precise timing of salt deposition in relation to the onset of seafloor spreading (Pindell et al., 2021; Salvador, 1991; Snedden et al., 2018). Initially, the age of the Louann salt and associated anhydrites was assumed to be Callovian (~162 Ma) based on the age of the overlying Norphlet Formation and Oxfordian Smackover Carbonate (Salvador, 1991). However, strontium (Sr) isotopes suggest an older age of 169–170 Ma (Pindell et al., 2021). The deposition of the such salt is believed to have occurred rapidly, taking less than a million years (Warren, 2006). This estimation finds support from numerical models of similar salt deposition in the South Atlantic and stratigraphic analyses of the Santos Basin in Brazil (Montaron & Tapponnier, 2009). Moreover, present-day observed rates of salt deposition in known areas (see Davison et al., 2012) align with the suggestion of rapid deposition in the GoM. Nevertheless, such rapid salt deposition is only possible with rapid subsidence during salt deposition (Davison et al., 2012). Some authors (Hudec et al., 2019; Pindell et al., 2021) propose an alternative interpretation,

suggesting that the salt may not represent a syn-rift deposit, but rather could have been deposited after the onset of oceanic spreading. This possibility is consistent with the absence of rift faults in observed seismic horizons of salts from the GoM (Horn et al., 2016). Alternatively, it is plausible that the salt deposition coincided with the onset of seafloor spreading (Lundin & Doré, 2017).

2.7. Seafloor spreading

The timing of seafloor spreading initiation and the nature of the crust beneath the salt layers in the GoM have been the subject of extensive research and debate (Escalona et al., 2021; Marton & Buffler, 1994; Minguez et al., 2020; Pindell, 1985; Pindell & Kennan, 2009). Various models have been proposed, relying on seafloor spreading rates and geophysical observations to determine the timing of seafloor spreading. For instance, satellite gravity data and the Extinct Spreading Ridge magnetic anomaly (ESRA; Figure 2) have been used to constrain the rotation of the Yucatán block with spreading rate estimations from the known East Coast magnetic anomaly (ECMA) and Blake Spur magnetic anomaly (BSMA) in the Central Atlantic (Marton & Buffler, 1994; Pindell et al., 2021; Pindell & Kennan, 2009). The asymmetry in the crust's nature on either side of the ESRA has led to different explanations. For example, Filina and Beutel (2022) proposed two phases of seafloor spreading with ridge reorganisation in between each phase. Similarly, Pindell et al. (2021) also suggested a two-phase spreading without ridge reorganisation. Another hypothesis suggests that mantle exhumation in the northeastern region of the GoM, followed by symmetrical oceanic spreading, could explain the asymmetry (Minguez et al., 2020). Observations of minor magnetic anomalies called En Echelon anomalies (EEA) by Minguez et al. (2020) align with the start of seafloor spreading, indicating some level of symmetry in the GoM's structure during the breakup (Figure 2). However, these anomalies were interpreted as a peridotite ridge rimming the oceanic crust rather than direct evidence of spreading (Minguez et al., 2020). Additionally, seismic reflection data in the central to northeastern GoM and along the Yucatán margin reveal ridge-like basement highs, interpreted as a mechanical boundary between the crust and mantle, allowing for mantle exhumation (Minguez et al., 2020; Pindell et al., 2014). These basement highs are bordered on the outside by the outer trough, which exhibit a drop in basement height by ~2 km adjacent to the inferred oceanic crust (Figure 2; Hudec et al., 2019). The trough and basement high are related to a regional magnetic low and a set of EEA magnetic anomalies, respectively. The presence of ridge-like basement high along with outer trough point to a magma-poor evolution of GoM. Continuation of these EEA anomalies in the western region of the GoM is marked by the BAHA high, which exhibits 3 km of relief in seismic data, but the magnetic anomaly signature is not very clear. The BAHA high has been interpreted to have formed at the same time as the deposition of salt, but the nature of the crust is still debated (Hudec & Norton, 2019). Initial interpretations (Fiduk et al., 1999) assumed it to be older oceanic crust formed during an early stage of spreading, while others propose hyperextended continental crust or exhumed mantle (Pindell et al., 2021). Hudec et al. (2019) proposed that the BAHA high might be a volcanic ridge that formed before seafloor spreading but after the salt deposition (since salt onlaps onto the BAHA high).

The GUMBO seismic imaging also revealed lateral variations in crustal composition across the northern GoM and identified two distinct crustal zones within the oceanic domain (Figures 4 and 5). GUMBO3 led to an interpretation of a two-layered structure with a basaltic upper layer and a gabbroic layer beneath, reaching a thickness of up to 9 km (Eddy et al., 2014). In contrast,

GUMBO4 imaged a thinner oceanic crust, around 5 km thick, with a uniform composition, suggesting limited magma supply during its formation (Christeson et al., 2014; Minguez et al., 2020). The presence of SDRs and coincident HMA, CMA, and other high magnetic anomalies led to suggestion of a magma-rich nature of GoM evolution (Filina & Hartford, 2021) but on the other hand presence of EEA, outer trough, and ridge-like basement high, points towards a magma-poor origin of GoM (Minguez et al., 2020; Pindell et al. 2016).

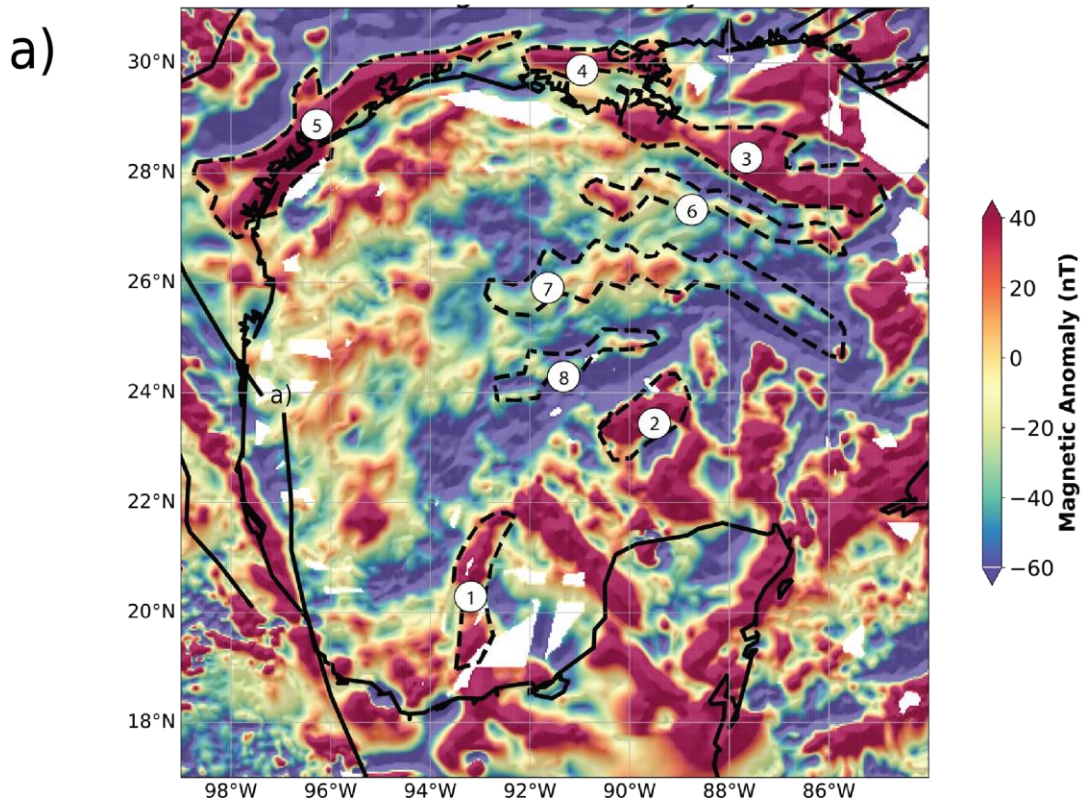
a)
30°N
28°N
26°N
24°N
22°N
20°N
18°N
98°W
96°W
94°W
92°W
90°W
88°W
86°W
1
2
3
4
5
6
7
8
a)
40
20
0
−20
−40
−60
Magnetic Anomaly (nT)

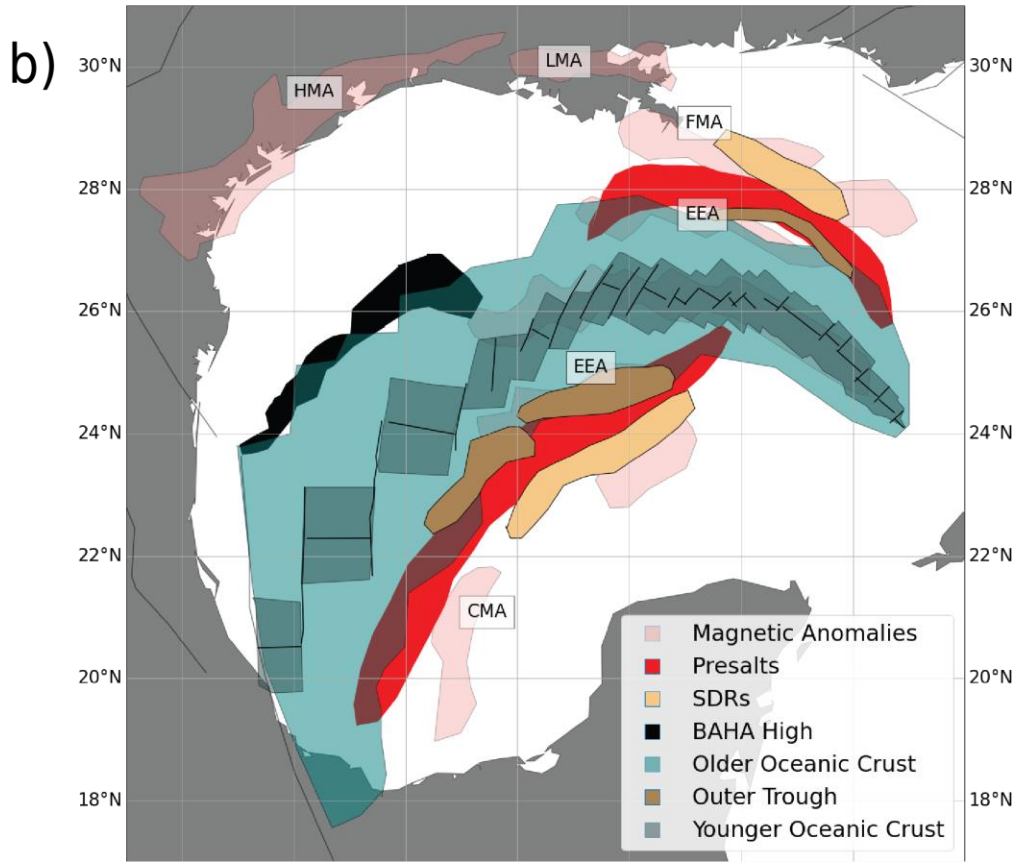
b)
HMA
LMA
FMA
EEA
EEA
CMA
Magnetic Anomalies
Presalts
SDRs
BAHA High
Older Oceanic Crust
Outer Trough
Younger Oceanic Crust

374

Figure 2. a) Magnetic anomaly map of the region (Meyer et al., 2017) showing important magnetic high (shaded black lines from Minguez et al., (2020) : (1) is the Campeche magnetic anomaly (CMA) (2) is the Yucatán magnetic anomaly (YMA) (3) is the Florida magnetic anomaly (FMA) (4) is the Louisiana magnetic anomaly (LMA) (5) is the Houston Magnetic Anomaly (HMA) 6) and 8) are En Echelon anomalies (EEA) and 7) is the Extinct Spreading Ridge Anomaly (ESRA). b) An illustration of the important geophysical interpretations in the region compiled from different sources. The presence of SDRs aligning with significant magnetic anomalies suggests a strong association with rift-related magmatism in the eastern GoM. The HMA, LMA, and CMA all are characterised by similar long-wavelength, rounded, or oblate-shaped anomaly pattern. The HMA and CMA likely indicate volcanic flows formed within the syn-rift sections of rift basins (Mickus et al., 2009), although confirming their nature is challenging due to their considerable burial depth. Notably, these anomalies and SDRs are not located at the transition to the oceanic crust. Another magnetic feature called EEA consists of smaller magnetic highs. Based on analog rock properties modelling, the EEA suggests the existence of a narrower zone of exhumed serpentinised mantle along the eastern GoM (Minguez et al., 2020). Seismic reflection data have revealed presence of ridge-like basement highs, interpreted as a mechanical boundary between the crust and mantle, facilitating mantle exhumation (Minguez et al., 2020; Pindell et al., 2014). These basement highs correlates well with the set of EEA magnetic anomalies. Moreover, these basement highs are bordered by the outer trough, which exhibits a deepening of the basement by 2 km adjacent to the inferred oceanic crust. BAHA high located in western GoM indicates a relief of 3 km in seismic data, the magnetic anomaly signature is less distinct here. The origin of the BAHA high is still debated, with some initial interpretations suggesting it to be older oceanic crust formed during an early stage of spreading, while others propose hyperextended continental crust or exhumed mantle (Hudec & Norton, 2019; Pindell et al., 2021; Hudec et al., 2019). The older and younger oceanic crust interpretation is based on Pindell et al. (2021)

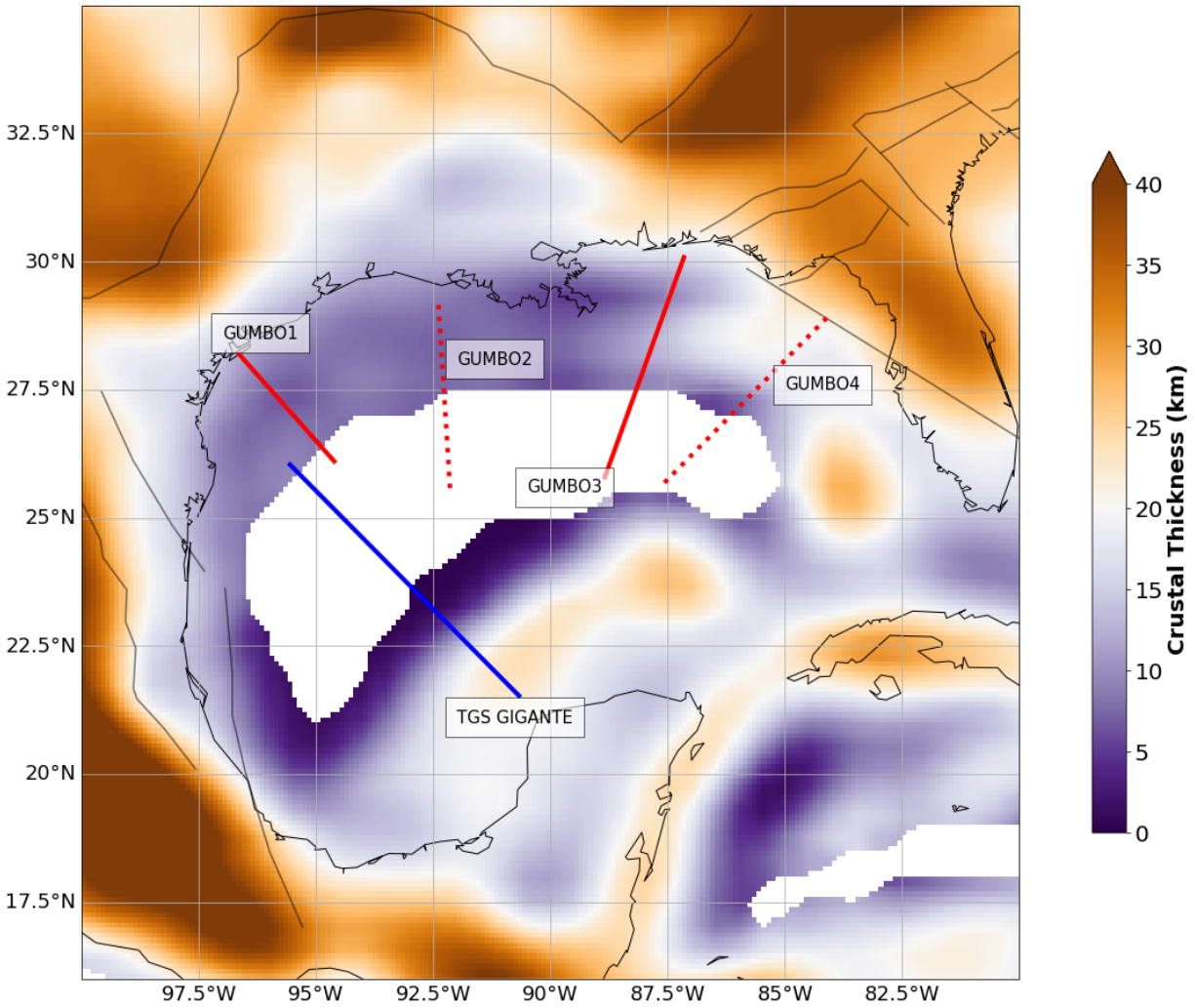

Figure 3. GEMMA crustal thickness model (Reguzzoni & Sampietro, 2015). The profiles marking the GUMBO experiments referred to in this study are depicted as red solid and dashed lines (Christeson et al., 2014; Eddy et al., 2018, 2018; Van Avendonk et al., 2015). GUMBO1 lies along western GoM while GUMBO3 and GUMBO4 is along eastern GoM. GUMBO2 lies in central GoM. The TGS GIGANTE line from Filina & Beutel (2022) is depicted as a blue line.

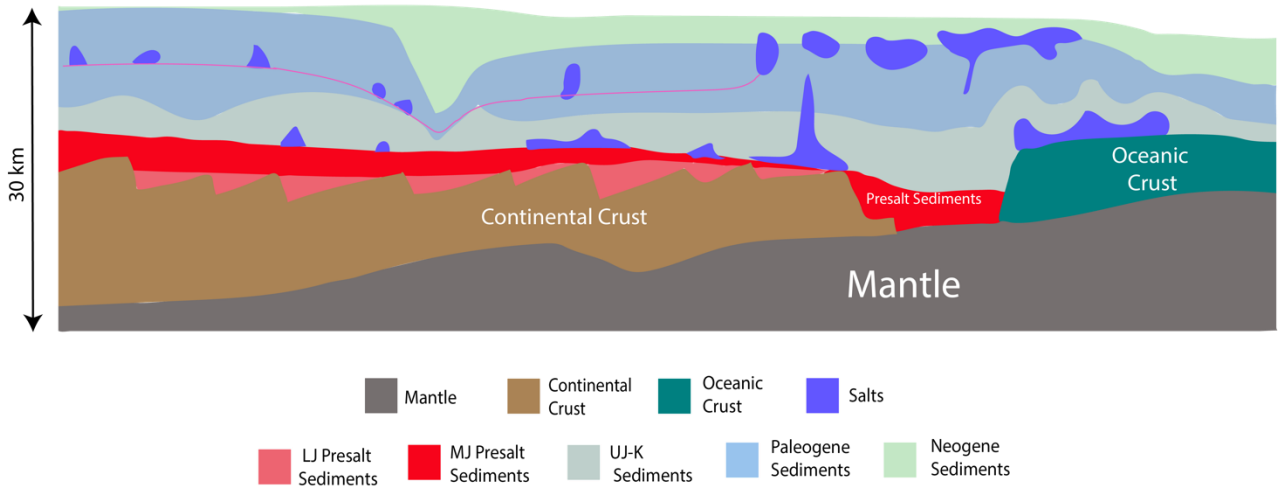

Figure 4. GUMBO1 line interpretation derived from Van Avendonk et al. (2015). The western GoM has a hyperextended continental crust with possible exhumation. Van Avendonk et al. (2015) interpreted high-velocity structure beneath the salt as pre-salt sedimentary deposits along western GoM. However, the presence of salt makes it difficult to perform detailed seismic imaging. An alternative interpretation of possible "salt wall" instead of these red beds is presented by Filina (2019).

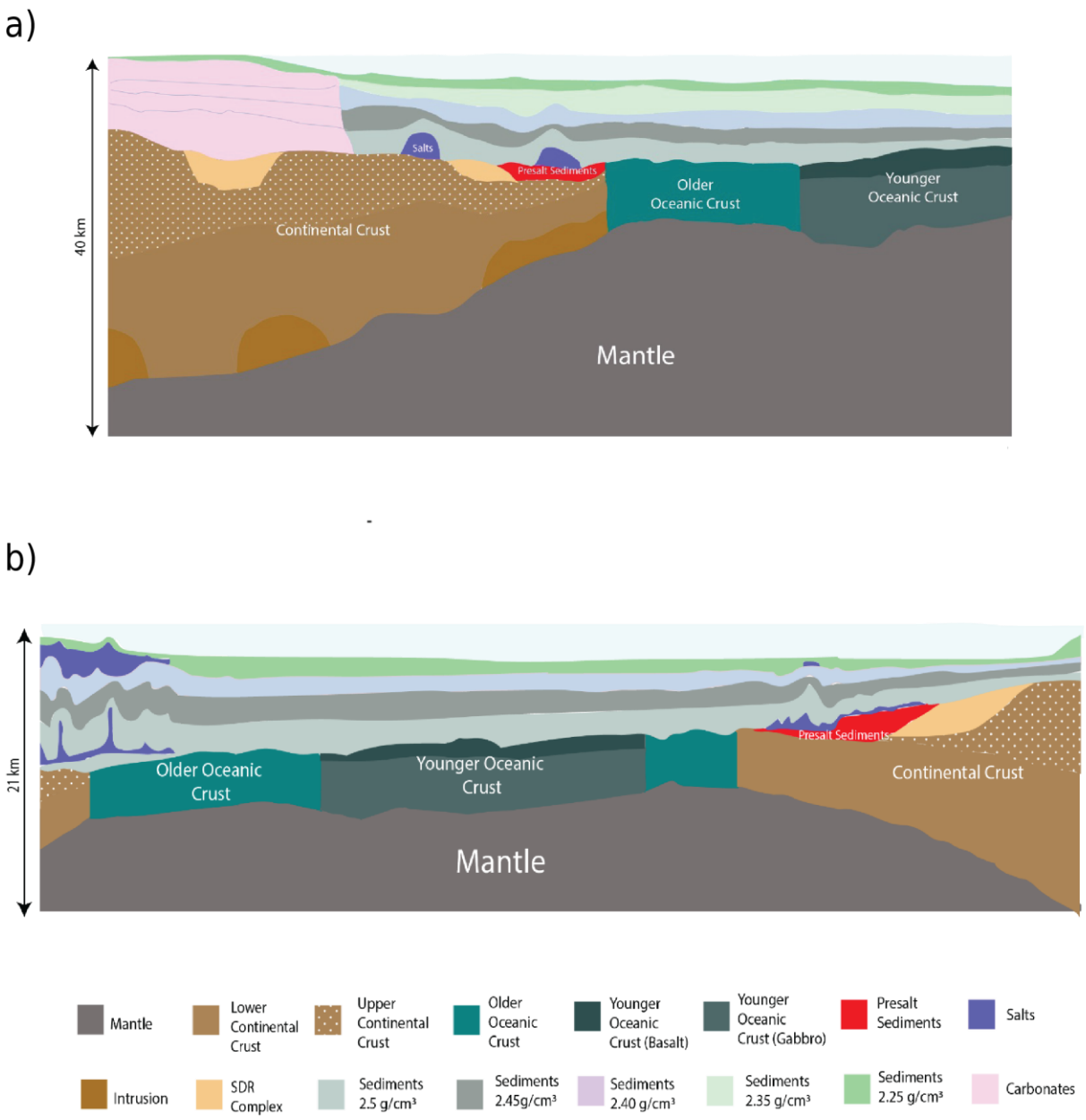

Figure 5. a) GUMBO3 line, and b) TGS GIGANTE line interpretations taken from Filina & Beutel (2022).

The Mesozoic geological history of the GoM poses significant challenges in tectonic reconstructions, demanding a comprehensive understanding of a range of complex factors. The large region of extensional deformation that has shaped the GoM necessitates a fresh approach to reconstructing the region. By addressing these challenges and adopting a comprehensive approach, one that incorporates a focused deformation approach, we can advance our understanding of the complex processes that have shaped the GoM and contribute to refining the tectonic reconstruction of this region.

3 Methodology

Traditional numerical approaches in plate tectonic reconstructions primarily focused on rigid plate motions, often neglecting the deformation of the plates themselves (Boschman et al., 2014; Müller et al., 2016; Pindell et al., 2021; Pindell & Kennan, 2009; Seton et al., 2012). However, a more recent global plate tectonic reconstruction model has emerged, introducing a novel methodology that incorporates deforming regions at plate boundaries through the establishment of deforming topology networks (Müller et ., 2019). To implement this approach, the deforming network is discretised into constant strain rate spherical triangular elements, utilising the Delaunay triangulation technique (Gurnis et al., 2018). By expressing the relative motion and velocities of the triangulation nodes within the deforming areas as finite rotations it becomes possible to calculate the strain rate associated with deformation at plate boundaries (Müller et al., 2019).

$$\dot{S} = \nabla . \overrightarrow{u} = \dot{\varepsilon}_{\mathrm{D}} \tag{1}$$

$\dot{S}$ is the strain rate; $\overrightarrow{u}$ is the velocity of points and $\dot{\varepsilon}_{\mathrm{D}}$ is the dilatation strain rate.

Furthermore, this methodology allows for the estimation of the finite strain history of points within these deformation zones, enabling the calculation of crustal thickness over time. By employing the governing equations, the temporal variations in crustal thickness can be utilised to derive the tectonic subsidence of passive rift margins. This integrated approach provides a more comprehensive understanding of the dynamic passive rift evolution.

3.1 Modelling Crustal Thickness

The evolution of passive rift margins hinges upon the process of crustal thinning. By considering the incompressibility of the lithospheric block, the mass conservation equation can be employed to depict the time-dependent evolution of crustal thickness. This assumes that there is no net mass generation or loss during the deformation process, with horizontal divergence or convergence governing the vertical thinning or thickening (Gurnis et al., 2018; Müller et al., 2019). Hence, the crustal thickness at any time *t* can be calculated using equation 2.

$$\frac{DH}{Dt} = -H . \dot{S} \tag{2}$$

where H is the crustal thickness and $\dot{S}$ is the strain rate.

3.2 Modelling Tectonic Subsidence

Basin formation arises from the stretching of the continental lithosphere and is part of a broader continuum encompassing continental rifting, passive margin development, and the emergence of

a new oceanic crust (Brune et al., 2023; Şengör & Natal'in, 2001). Over geological timescales, the process of rifting culminates in the thinning and formation of passive margins, with seafloor spreading commonly commencing when the stretching factor (β) surpasses a critical threshold (Le Pichon & Sibuet, 1981). The β can be expressed as:

$$\beta = \frac{H_i}{H} \tag{3}$$

where H_i and H are the initial crustal thickness and crustal thickness at time t, respectively.

The isostatic adjustments stemming from lithospheric processes triggered by such stretching are reflected in subsidence histories, which offer insights into the mechanisms driving basin formation. Under the assumption of local isostatic equilibrium, the evolution of passive continental margins can be elucidated by McKenzie's (1978) stretching model. According to this model, the present-day depth of the seafloor at any point within a rift is contingent upon the timing and duration of rifting, the elapsed time since rifting cessation, and the stretching factor (β). Nevertheless, stretching alone does not govern tectonic subsidence (McKenzie, 1978). Subsidence analysis of most passive rift margins worldwide reveals that subsidence occurs through a combination of mechanisms. Initially, subsidence arises from rifting and extension of the continental crust and also due thermal anomaly from upwelling of asthenosphere. After the stretching ceases subsidence it is characterised by a slower diffusive decay of thermal anomaly which will further produce a thermal subsidence attributable to the gradual cooling and rethickening of the stretched lithosphere (Jarvis & McKenzie, 1980).

For our model, the subsidence due to the extension (TS_1) can be calculated using the thinning factor.

$$\mathrm{TS}_1 = A\left(1 - \frac{1}{\beta}\right) \tag{4}$$

However, the loss of heat and thermal subsidence actually commences during the extension phase and needs to be considered simultaneously to obtain a realistic estimate of syn-rift extension (Jarvis & McKenzie, 1980). Therefore, slow thermal subsidence (TS_2) can be calculated by estimating temperature evolution using the advection-diffusion equation 6.

$$TS_2 = B \int_0^{L_c} (T'(z) - T(\mathrm{z})) \tag{5}$$

where T' and T are steady state (equation 6) and initial temperature, L_c is the thickness of the lithosphere, and z is the depth from the surface.

$$\frac{dT}{dt} = \kappa \frac{d^2T}{dz^2} - v(z)\frac{dT}{dz} \tag{6}$$

The thermal diffusivity κ represents how heat spreads in a material. The vertical velocity, denoted as $v(z)$, arises from stretching effects. At the top surface (where z=0), the vertical velocity is zero. At the bottom surface (where z=L_c), it is represented as -V_0 and varies linearly with depth (z).

A and B are constant ratios that depend on the density of crust (ρ_c), mantle(ρ_m), asthenosphere (ρ_a), and thermal expansion coefficient (α) and calculated as follows

$$A = \frac{(\rho_m - \rho_c)}{(\rho_a - \rho_w)} L_c \tag{7}$$

$$B = \frac{\alpha \rho_m}{(\rho_a - \rho_m)} \tag{8}$$

It is worth noting that our subsidence model does not account for factors such as sediment accumulation and loading, orogenic loading, salt tectonics or subsidence due to dynamic topography.

3.3. Focused Deformation

Conventional models for crustal stretching typically assume uniform thinning and constant strain throughout the deformable zone when calculating crustal thickness and tectonic subsidence (Müller et al., 2019). However, this assumption does not hold true in many geological scenarios. Asymmetric subsidence patterns are commonly observed in basins during the rifting and breakup phase, resulting in enhanced subsidence towards the seaward side of the hinge zone (Huerta & Harry, 2012; Xie & Heller, 2009). This is because of focused extensional strain distribution, which can be attributed to brittle and ductile weakening processes (Brune et al., 2023). For instance, lithospheric “necking” can cause localised thinning by a large-scale thermal weakening process that transforms the originally cold and strong lithosphere into a hotter and weaker mantle (Chenin et al., 2018). Variations in crustal strength and viscosity can also lead to uneven deformation, resulting in focused zones of deformation (Bott, 1992; Ebinger et al., 2017). To accurately capture these complexities, numerical models incorporating non-uniform thinning and variable strain distributions are necessary. To address this, a modified extension model based on Jarvis & McKenzie, (1980) can be employed to calculate the tectonic subsidence of the passive margin during initial rifting, integrating the concept of focused deformation within the deforming plate motion model (Figure 6a).

In the focused deformation model, stretching factors evolve over time, initially exhibiting a more uniform distribution and exponentially increasing seaward until continental rupture and oceanic

crust formation occurs. Our method allows for the control of the spatial variation of strain rate in a rift profile by varying the **exponential stretching coefficient** (C) parameter while ensuring that the network triangulation is sub-divided to fit the exponential curve within a certain tolerance specified by the rift strain rate resolution and rift edge length threshold. The rift strain rate resolution parameter is used to determine when rift edges in network triangulation need to be subdivided to match the exponential curve within a certain tolerance. However, the sub-division is also limited by the rift edge length parameter, which specifies the minimum length (in degrees) of the rift edges that will not be further subdivided, controlling the spatial variation of strain rate perpendicular to the rift profile (Figure 6b and 6c). The strain rate along the rift profile can be represented as:

$$\dot{\varepsilon}(x) = \dot{\varepsilon_0} \cdot e^{cx} \cdot \frac{c}{(e^c - 1)} \tag{9}$$

where $\dot{\varepsilon_0}$ is undivided strain rate, c is the exponential stretching coefficient, and x is normalised distance which is 0 at the unstretched point and 1 at the stretched point.

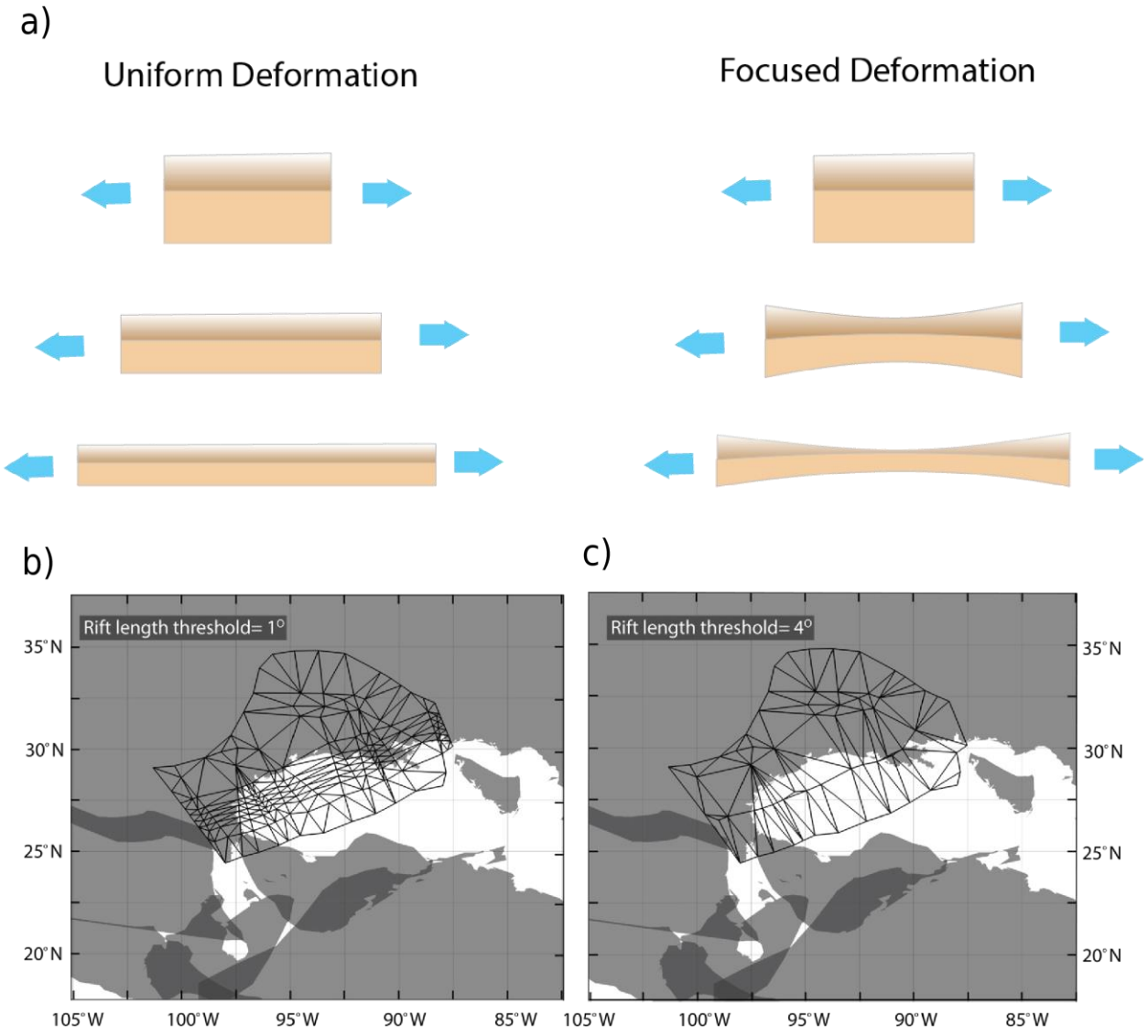

Figure 6. a) Model showing the difference between uniform and focused deformation where the top layer represents the crust, and the bottom layer represents the lithospheric mantle. **b-c**) Deformation topology network (black mesh) used in this study and comparison of parameters showing how rift length threshold is used to divide the strain rate in the deformation mesh. The figure (b) has a rift length threshold value of 1.0, while (c), have a rift length threshold value of 4.0. The **strain rate resolution** parameter guides the decision on when to subdivide the network (in perpendicular to the rift direction) to match the exponential curve within a certain tolerance, hence controlling the strain rate perpendicular to the rift. The **rift edge length threshold** parameter further controls the division of the topological network. The minimum possible element length of topological network cannot be less than this parameter, thereby governing the non-uniform spatial variation of strain rate. Grey blocks refer to rigid continental block, which overlaps in the regions of tighter pre-Pangea fit which have also undergone deformation. However, these regions are out of scope for this study.

3.4 Optimising the Model

Our numerical model relies on a set of initial conditions and model parameters (Table 1) that must be determined to reconstruct the stretching factor, crustal thickness, and tectonic subsidence history. Of utmost importance are the deformation topology network between the Yucatán and North America blocks, which defines the extension region, and the relative plate motions between the blocks, which serves as the primary input variables for our model.

To create a deforming plate reconstruction, it is necessary to delineate the boundaries between the deforming and rigid areas (Figure 6b & c; Müller et al., 2019). This requires thorough geological and regional investigations to ascertain the extent of the deformation zone in the geological past, which ultimately influences the overall distribution of strain rates at the plate boundaries. Considering that the motion between the Yucatán and North America blocks drives GoM tectonics, we constructed the deformable plate model utilising these blocks only (Marton & Buffler, 1994). While deformation in Mexico and Florida was active during the syn-rift phase (Pindell et al., 2021), we focused the deformation mesh on the GoM Basin treating Mexico and Florida as rigid blocks. The eastern boundary of our deforming zone is defined by the Burgos Lineament and Western Transform margin (Figure 1). The southern boundary is demarcated by the Yucatán block; however, in our reconstruction, the Chiapas block was not part of Yucatán until the Valanginian times (Pindell et al., 2021). The northern limit of our deformation zone is determined by the Ouachita-Marathon thrust belt and Triassic mid-rift high (Dickinson et al., 2010; J. W. Snedden & Galloway, 2019). Estimating the precise shape and location of the mid-rift high in the Triassic is challenging, but it can be inferred from the present-day Sabine Uplift, the primary GoM rift basin, and the deposition pattern of the Louann salt (Salvador, 1991; J. W. Snedden & Galloway, 2019). In our reconstruction, we introduced fixed non-deforming nodes around the Sabine Uplift to encompass this region. Furthermore, we fined tuned the fixed non-deforming nodes around these areas by matching the calculated crustal thickness from our model with known estimates from the GEMMA model (Reguzzoni & Sampietro, 2015).

Table 1. Parameters used in this study in generating our optimised deforming model. The crustal density values are derived from density calculations of GUMBO1 and GUMB02, as detailed in Filina (2019). The density of water is referenced from Smith & Sandwell (1997), while the mantle density is taken from Zoback & Mooney (2010). For the purposes of this study, a standard lithospheric thickness of 125 km is assumed, in accordance with the thickness estimate derived from the shear wave velocity model within the unextended region (131 ± 28 km; Ho et al., 2016). It is worth noting that the lithospheric thickness within the GoM region exhibits variability in the present day. This variability is reflected in estimated thicknesses of 87 km in the oceanic domain and greater than 100 km in the northern GoM which due to extension and cooling (Nguyen et al., 2022).

Parameters	**Values**
Initial Crustal Thickness (H_i)	Constant for optimizing
Lithospheric Thickness (L_c)	125 Km
Density of Crust (ρ_c)	2800 kg/m^3

Density of Mantle (ρ_m)	3330 kg/m^3
Density of water (ρ_w)	1030 kg/m^3
Exponent Stretching Factor (C)	Constant for optimizing
Rift Length Threshold	Constant for optimizing
Strain Rate Resolution	Constant for optimizing
Thermal Expansion coefficient (α)	3.28e-5 $^oC^{-1}$
Thermal Diffusivity	8.04e-7 m^2/s

A second crucial input for our reconstruction is the relative plate motion between North America and Yucatán. Various regional and global plate models can be employed, and their results can be compared to recent observations (Boschman et al., 2014; Müller et al., 2019; Pindell & Kennan, 2009; Seton et al., 2012). We adopted Kneller and Johnson's (2011) plate reconstruction model, which proposes a close fit of North America and Yucatán plate to restore the original position of Yucatán prior to the rift-to-drift transition at ~195 Ma. This plate reconstruction model is based on the restoration of crustal thickness and refraction lines. To model the rift-to-drift transition, we assessed the flowlines generated by three different plate reconstruction models (Table 2). Each model offers distinct interpretations of the history and processes that contributed to the formation of the GoM (Table 1). Pindell et al. (2021), based on proprietary magnetic data, propose one stage of continental rifting and two phases of oceanic spreading. It suggests a syn-drift change in the position of the pole of rotation approximately 150 Ma and includes a potential episode of mantle exhumation. Minguez et al. (2020) utilises gravity data to derive plate motions and magnetic data to determine the timing and location of seafloor spreading. According to this model, the GoM opened as a rift between South and North America, with seafloor spreading commencing in the west and propagating eastward, concluding around 154 Ma. The Filina and Beutel (2022) model, which integrates potential fields and seismic data, also proposes two phases of oceanic spreading, with ridge propagation occurring approximately 151 Ma. Pre-drift positions of the Yucatán block are defined using SDRs. This model suggests temporal variability in the magmatic regime during GoM opening, ranging from CAMP (~200 Ma) to initial amagmatic ultra-slow spreading (~165 Ma) followed by a faster magmatic phase of spreading (~152 Ma). We compared the flowlines of these three models using the vertical gravity gradient (VGG) grids data (Sandwell et al., 2021) based on two visible curvilinear rotation fabrics and an extinct spreading centre. Based on closer match of these curvilinear rotation fabrics with flowlines generated by Pindell et al. (2021) model, we selected it to be the most suitable input model for our reconstruction.

Table 2. Summary of the models assessed in this study, documenting the timing, opening phase, and constraints used.

Model	**Timing**	**Comments**

Pindell et al. (2021)	195–167 Ma	**Reconstruction**: Start of the rift to drift transition. **Constraints:** CMA and HMA will be parallel to each other
	169 Ma	**Reconstruction**: Deposition of salt (based on recent Sr-isotope data)
	167–147 Ma	**Reconstruction**: The first phase of seafloor spreading. **Constraints:** The northern and southern anomaly trends (NMAT and SMAT) are interpreted as a transition between the exhumed mantle and oceanic crust.
	147–137 Ma	**Reconstruction**: The second phase of seafloor spreading. **Constraints:** Central magnetic anomaly trend (CMAT) interpreted as the youngest oceanic crust
Minguez et al. (2020)	203–169 Ma	**Reconstruction**: Syn-rift Phase **Constraints:** Subparallel opening to the South America plate
	170 Ma	**Reconstruction**: Deposition of salt
	169–166 Ma	**Reconstruction**: Exhumation of the mantle. **Constraints:** EEA and its conjugate are collinear.
	166–154 Ma	**Reconstruction**: Seafloor spreading. **Constraints:** ESRA can be produced by full spreading rate of 2.4 cm/year with Chron M2n at the extinct spreading center.
Filina and Beutel (2022)	220–169 Ma	**Reconstruction**: Syn-rift Phase. **Constraints:** SDRs on the Yucatán and North American margins should be near each other.
	169 Ma	**Reconstruction**: Deposition of salt
	169–165 Ma	**Reconstruction**: Post-continental stretching **Constraints:** Presence of Outer Trough on the northern Yucatán margin
	165–152 Ma	**Reconstruction**: First spreading phase **Constraints:** Thin and uniform oceanic crust

	152–135 Ma	**Reconstruction**: Second spreading phase Thick and layered oceanic crust

In our approach, we employ pyGPlates (www.gplates.org) to forward model the evolution of crustal thickness up to the present day, utilising the plate rotation and deforming topological network as primary inputs. To ensure the accuracy of our model, we compare the calculated crustal thickness at 0 Ma (present day) with the present-day crustal thickness estimates from known GEMMA crustal thickness model (Reguzzoni & Sampietro, 2015). This comparison allows us to search for optimal values of key parameters, including the edge length threshold, strain rate resolution, and exponential stretching factor used for the distribution of strain rates in passive rift margins. By achieving the closest match with the present-day crustal thickness, we can identify the most suitable values for these parameters and enhance the reliability of our reconstruction. Yet another critical input parameter for modelling the evolution of crustal thickness over time is the initial crustal thickness. The area where passive margins extend landward is determined by the limit of the continental crust before significant stretching occurs, referred to as the unstretched continental crust limit (UCCL; Nemčok, 2016). Initially, a range of crustal thickness can be estimated based on UCCL and subsequently refined during optimisation along with other parameters. This optimisation process enables us to refine our understanding of the crustal thickness evolution and its implications throughout the studied time span. Specifically, we examined 12,870 combinations of the exponential stretching coefficient, rift threshold length, strain rate resolution, and initial crustal thickness to find the optimal configuration for our study. To evaluate the performance of each model, we utilised the minimum Root Mean Square Error (RMSE) as our benchmark, comparing the calculated crustal thickness at 0 Ma with the present-day GEMMA crustal thickness. This metric effectively penalises outliers, providing a comprehensive assessment of model accuracy.

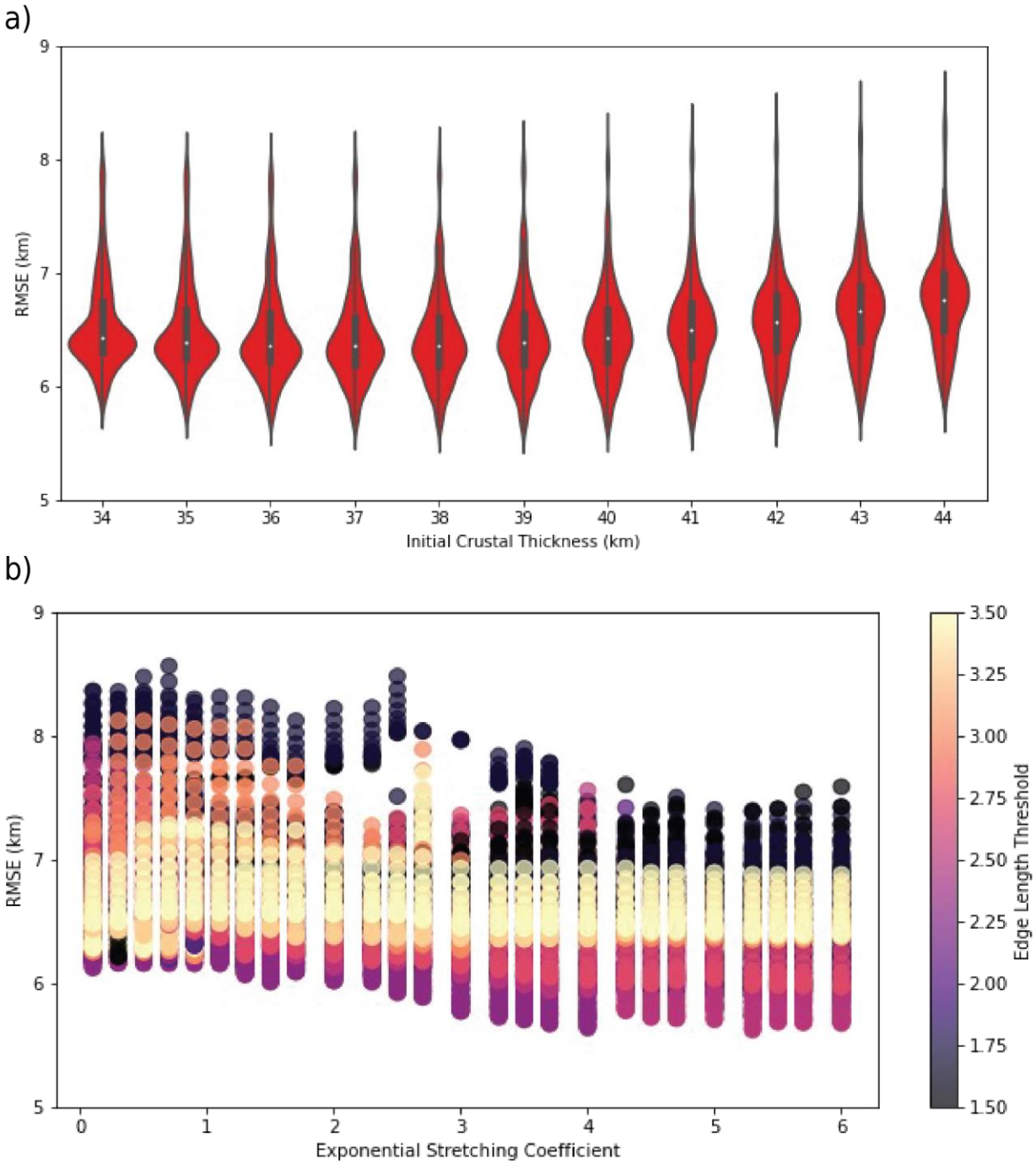

Figure 7. Results from our optimisation of 12870 combinations of the exponential stretching coefficient, rift threshold length, strain rate resolution, and initial crustal thickness. We used Root mean squared error (RMSE) calculated between crustal thickness estimates at 0 Ma and known GEMMA crustal thickness model (Reguzzoni & Sampietro, 2015) as our performance metric. Our optimisation results show that initial crustal thickness and exponential stretching coefficient are the primary factor controlling model performance. a) RMSE for different values

of initial crustal thickness b) RMSE for different exponential stretching coefficient and edge length threshold.

4 Results

4.1. Optimisation

Analysis of the variation of RMSE with varying values of crustal thickness, exponential stretching coefficient, and Edge Length Threshold revealed that the initial crustal thickness and exponential stretching coefficient had the most significant impact on our model's performance (Figure 7). Through testing, a global minimum model with an RMSE of 5.6 km was found that had an exponential stretching coefficient of 5.3 and an estimated initial crustal thickness prior to GoM stretching of 39 km. The crustal thickness estimates based on UCCL suggest a thickness of 38.4 ± 3.0 km for unstretched crust (Hosseinpour et al., 2013; Kaban et al., 2014; Reguzzoni & Sampietro, 2015), which closely aligns with the optimized value obtained from the model. Notably, the edge length threshold and strain rate resolution parameters, crucial for achieving the closest match, fell consistently within the ranges of 2.25 to 2.75 and 10^{-16} to 10^{-17}, respectively. When comparing our model with the uniform deformation model proposed by Müller et al. (2019) for the same region, we found that our focused deformation model's RMSE outperformed it by nearly 2.5 times in estimating crustal thickness. Additionally, our model exhibited excellent agreement with the GEMMA crustal thickness model (Reguzzoni & Sampietro, 2015), particularly in the eastern and western GoM regions, with an absolute error of ~1.5 km.

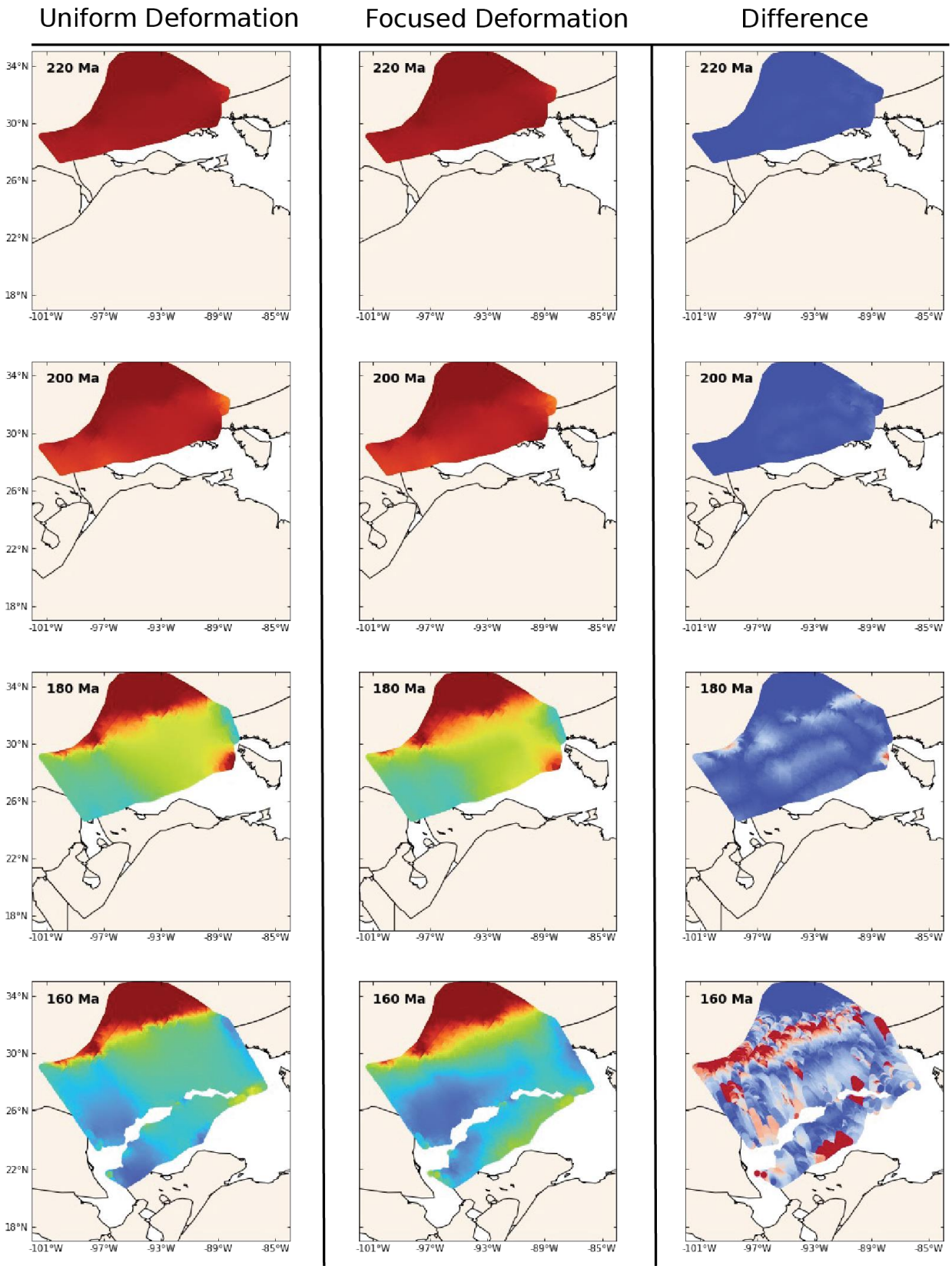
Uniform Deformation
Focused Deformation
Difference
220 Ma
200 Ma
180 Ma
160 Ma
34°N
30°N
26°N
22°N
18°N
-101°W
-97°W
-93°W
-89°W
-85°W

742
743
744

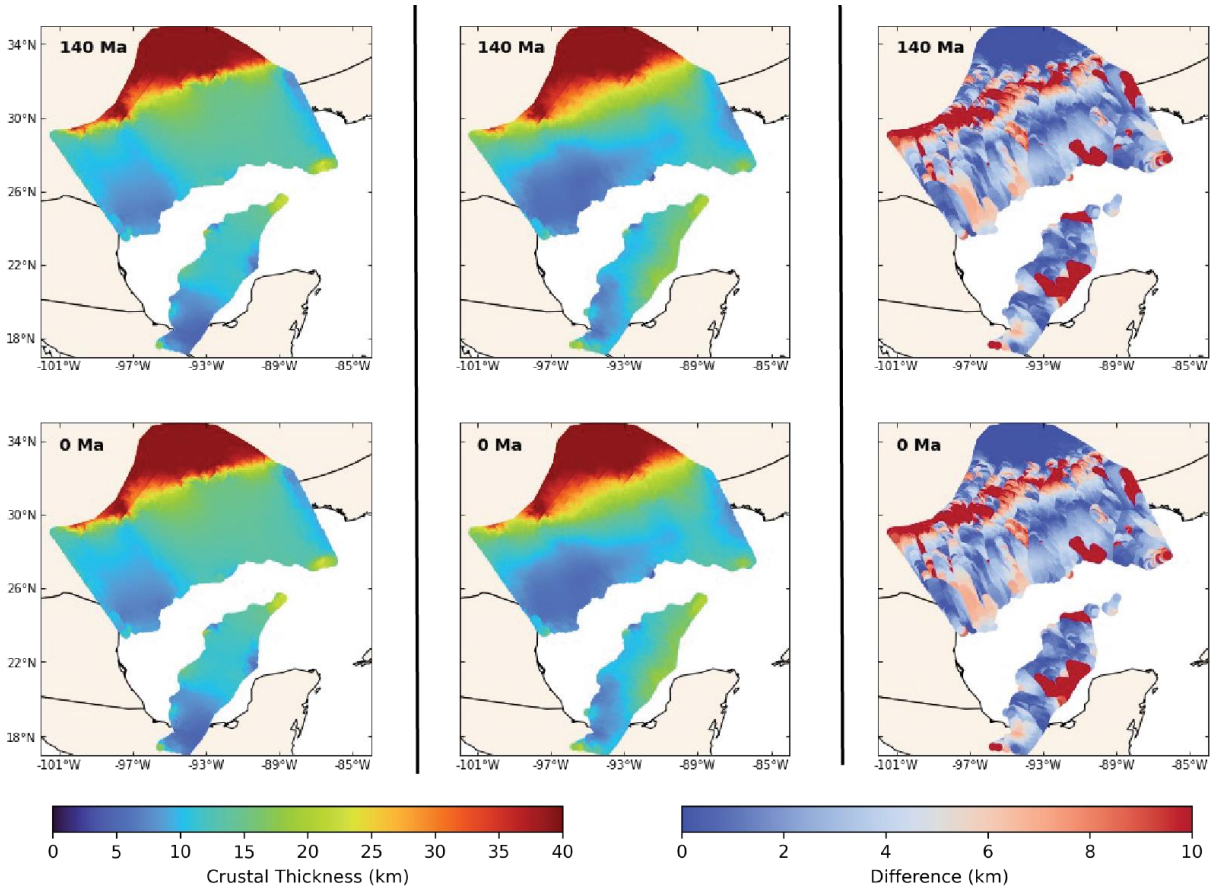

Figure 8: A comparison of crustal thickness between our uniform deformation model and focused deformation model, where colored region demonstrates deformed continental crust. During the early evolution from 230 Ma to 190 Ma, the crustal thickness shows similarities spatially in both the uniform and focused deformation scenarios. However, from ~190 Ma to ~175 Ma, a region of focused stretching emerges in the central GoM (see 180 Ma). Notably, there is a significant disparity in crustal thickness estimation between the focused deformation and uniform deformation models after the rifting event at ~160 Ma.

4.2 Evolution of stretching factor, crustal thickness, and tectonic subsidence

4.2.1 Early Triassic-Sinemurian (~230 Ma to ~190 Ma)

The initiation of continental rifting in the GoM traces back to the Triassic period when the Yucatán block was coupled with the South America plate. During this stage, some extension occurred between North America and Yucatán. According to our model, the region experienced approximately 120 km of extension before the Yucatán block began drifting and undergoing anticlockwise rotation. However, accurately determining the pre-rift position of the Yucatán block poses challenges due to limited means of estimating internal extension caused by rifting and the ongoing debate surrounding the definition of the Yucatán block itself. For instance, recent research has suggested that the Chuacús Complex, once considered part of Yucatán, is

allochthonous due to its distinct high-pressure, low-temperature metamorphic characteristics (Maldonado et al., 2018).

During the initial phase, the extension was relatively uniform along a north-south direction, characterised by minimal stretching ($\beta = 1.1$) and crustal thinning (Figure 8). The gradual stretching process resulted in the development of low strain rates ($6 \times 10^{-16} – 4.0 \times 10^{-16}\ s^{-1}$) evenly distributed across the region. However, tectonic subsidence calculations reveal lateral variation in the east-west direction, leading to the creation of accommodation for the deposition of Triassic sediments (Figure 9 and 10). The western GoM exhibited approximately 1.5 km of tectonic subsidence, gradually decreasing towards the central GoM (Figure 10). Similarly, the eastern GoM region adjacent to the SGR showcased a similar value (~1.2 km) of subsidence.

4.2.2 Pliensbachian-Toarcian (~190 Ma to ~175 Ma)

The opening of the Proto-Caribbean basin triggered the rotation of the Yucatán block, leading to significant extension of GoM continental crust. During this phase, our model indicates a rapid tectonic subsidence of 3–5 km between North America and Yucatán. However, the zone of stretching exhibits spatial variability. As the Yucatán block drifted southward, the strain rate within the deformation zone increased, from $4.0 \times 10^{-16}\ s^{-1}$ to $1.7 \times 10^{-15}\ s^{-1}$, resulting in more focused deformation in the region between blocks. Our model allows for the adjustment of the deformation mesh, concentrating the extension within the region of necking. Notably, our results highlight the development of a focused stretching zone that propagated from the western to eastern region of the GoM. In contrast, the uniform deformation model failed to capture this focused region of thinning, particularly in the central and eastern GoM (see snapshots 180 Ma and 160 Ma in Figure 8).

We find that rapid tectonic subsidence initiated in a wider zone in the western GoM and a narrower zone in the central and eastern GoM during the Pliensbachian period (~185 Ma) and then propagated to create a wider central and western GoM by the Bajocian period (~170 Ma). Tectonic subsidence reached approximately 4-5 km in the western GoM and 2-3 km in the eastern GoM, revealing lateral variations in the accommodation within the GoM prior to its opening (Figure 10). However, our model indicates that this heightened subsidence was confined to the region of focused stretching rather than being uniformly distributed across the basin. We observe significant stretching, with the β value transitioning from 1.1 at the start of the Early Jurassic to a value greater than 4 by the end of the Early Jurassic, resulting in substantial crustal thinning (Figure 11). Additionally, the overall stretching occurred in a wider zone in the western GoM compared to the central and eastern regions. Our crustal thickness calculation demonstrates that during the Pliensbachian period, the western GoM experienced considerable thinning, with an average thickness of 17 km, while the central and eastern regions of the GoM thinned to an average thickness of 26 km (Figure 8).

4.2.3 Middle-Late Jurassic (~175 Ma to ~145 Ma)

During the Toarcian to Callovian periods, the western GoM experienced substantial thinning due to the intensified extension caused by the anticlockwise rotation of the Yucatán block.

Consequently, the average crustal thickness in this region decreased to less than 10 km. Furthermore, the western GoM exhibited higher tectonic subsidence compared to the eastern region. Although extension in the western GoM ceased in the Callovian (~166 Ma), it persisted into the Early Oxfordian (~162 Ma) in the eastern GoM, albeit at a reduced rate (Figures 11 and 12). Considering the dominance of salt deposition during the Bajocian age and the limited influence of outer-margin extension on the base-salt layer near the oceanic crust margins, it is plausible to consider that the divergence of the northern GoM and Yucatán salt depocenters, as well as the initiation of seafloor spreading, occurred as early as the Bathonian epoch.

Our model indicates that the zone of focused stretching propagated from west to east prior to the onset of seafloor spreading. However, with the onset of seafloor spreading, our deformation model reveals a stage-wise opening process. It commenced in the Bathonian in the western GoM, followed by spreading in the central GoM during the Callovian and eventually reaching the eastern GoM by the Oxfordian. Notably, an intriguing observation from our model is that the seafloor spreading occurred south of the region of focused stretching, suggesting a possible rift jump. Additionally, the spreading center exhibited asymmetry in both the eastern and western GoM with respect to the focused stretching zone. However, in the central GoM, the spreading center was in close proximity to the region of focused stretching. By the Kimmeridgian period (~153 Ma), rotational seafloor spreading continued, accompanied by a similar but opposite rotational seafloor spreading in the Proto-Caribbean Seaway. The second phase of drifting commenced in the Tithonian, characterised by a gradually decreasing spreading rate.

4.2.4 Cretaceous

By the end of the Berriasian (~140 Ma), seafloor spreading in the GoM had significantly decelerated. In the early Valanginian stage, the Yucatán block had reached its current position relative to North America, indicating the possible completion of rotational seafloor spreading in the GoM. The subsequent separation between the North and South American plates took place exclusively within the Proto-Caribbean Seaway after this period. During this time, the GoM experienced crustal cooling and entered a phase dominated by thermal subsidence, creating ample space for the deposition of thick sedimentary layers. Following the extensional phase, gradual conductive cooling of the lithosphere occurred, leading to increased density in both the crust and mantle. In order to maintain isostatic equilibrium, the basin underwent gradual subsidence. Throughout much of the Cretaceous period, the GoM was characterised by passive tectonic conditions in most areas, with occasional localised interruptions caused by factors such as igneous activity and thermal uplift in the eastern Texas region surrounding the Sabine Uplift. Although these factors significantly influenced the tectonic subsidence of the basin, they could not be accounted for in our model.

5 Discussion

5.1. Initial rifting and red bed deposition

During the initial rifting phase prior to the anticlockwise rotation of the Yucatán block, our model indicates ~1.5 km of subsidence, which would have created accommodation for the deposition of red bed sediments. However, our tectonic subsidence calculation suggests that the

estimated thickness of red bed sediments from our model in the northern GoM is slightly lower than the inferred thickness (Milliken, 1988). This observation may imply that the deposition of red beds filled pre-existing accommodation spaces rather than depositing directly within a graben. It is important to note that our tectonic subsidence calculation relies on the stretching imposed by Yucatán motion, and we have limited constraints on the internal deformation of the Yucatán block and the position of the mid-rift high. Moreover, our model may not be able to capture high frequency, high amplitude changes in stratal thicknesses caused by brittle deformation which can also be responsible for thicker red beds in northern GoM. Nonetheless, our model offers valuable insights into how sediments might have been routed southward from the Ouachita-Marathon region.

The initial tectonic subsidence of ~1.5 km in the eastern and western parts of the GoM, between 230 Ma and 190 Ma before the drifting stage suggests that sediment deposition routes were bifurcated to the east and west within the narrow extensional zone between Yucatán and North America. This is further supported by the presence of interior drainage systems extending across various North American basement source terranes, as evidenced by diverse U-Pb age spectra from pre-salt wells (Frederick et al., 2020; Snedden & Galloway, 2019). Detrital zircon data from 16 wells show the existence of three distinct paleo drainage systems in the northern GoM (Frederick et al., 2020), which aligns well with our model (Figure 10). The western paleo drainage system extended from the highlands of Central Texas to the submarine Potosi Fan on the western margin of Laurentia. Detrital zircon ages from the Eagle Mills sediments in this region suggest tributary sources from the East Mexico arc, Yucatán/Maya, and Marathon-Ouachita provinces, encompassing a range of detrital zircon ages (Frederick et al., 2020). The southwestern flow was characterised by peri-Gondwanan detrital zircon ages from late Paleozoic accreted basement and/or successor basins, while the southeastern fluvial networks originated from traditional North American basement provinces, including Grenville, Mid-Continent, and Yavapai-Mazatzal. The southern paleo drainage system in the north-central GoM region is bifurcated around the Sabine and Monroe uplifted terranes (Figure 10). The eastern paleo drainage system exhibited a regional southward flow, with pre-salt detrital zircon ages predominantly indicating local Gondwanan/peri-Gondwanan sources, such as the proximal Suwannee terrane and Osceola Granite complex (Frederick et al., 2020).

Our model suggests that these paleo drainage systems likely served as the sources of basin fill in the GoM (Figure 10). The creation of accommodation in the western GoM facilitated the deposition of red bed sediments through the western paleo drainage system and the western branch of the bifurcated southern paleo drainage routes. Similarly, tectonic subsidence in the eastern GoM region would have also provided space for sedimentation in the eastern branch of the southern paleo drainage system and the eastern paleo drainage system.

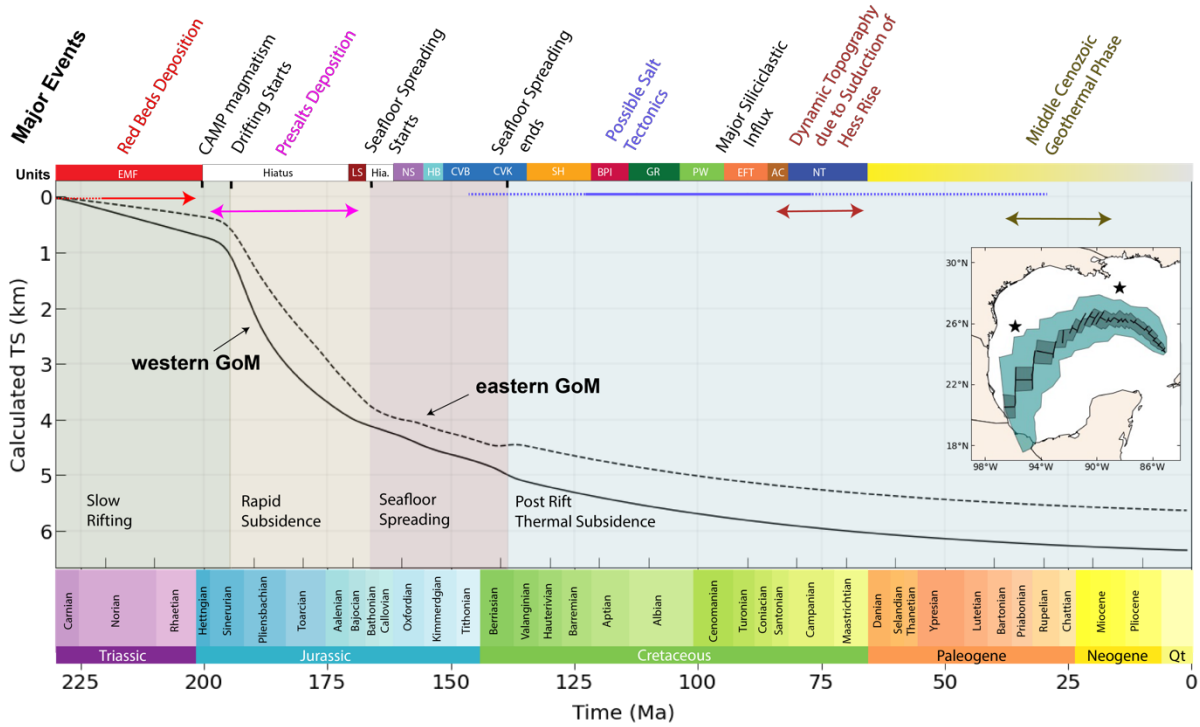

Figure 9. Tectonic subsidence calculation from our model. Four stages can be used to describe the tectonic evolution of the GoM basin. Slow rifting Phase: In this phase, there is small tectonic subsidence creating accommodation for infilling the GoM basin with red beds. Rapid Subsidence: Following the rift-drift transition, there is rapid subsidence which resulted in 3-4 km of subsidence. This led to the deposition of pre-salts. Seafloor Spreading Phase: The Louann salts have already been deposited. First, the western GoM opened, followed by the eastern GoM. Post-Rift Thermal Subsidence: The last stage is marked by conductive cooling of the lithosphere resulting in gradual tectonic subsidence. The difference in tectonic subsidence in western GoM and eastern GoM further increases. Most of the later secondary tectonic activity (Major events in color) would have influenced the tectonic subsidence and has not been accounted for in this study. Abbreviations: EMF, Eagle Mills Formation; LS, Louann Salt; NS, Norphlet-Smackover Formations; HB, Haynesville-Buckner Formations; CVB, Cotton Valley-Bossier; CVK, Cotton Valley-Knowles; SH, Sligo-Hosston; BPI, Bexar-Pine Island; GR, Glen Rose; PW, Paluxy–Washita; EFT, Eagle Ford-Tuscaloosa; AC, Austin Chalk; and NT, Navarro-Taylor.

5.2 Rapid subsidence and pre-salt deposition

The ~40 Myr hiatus between the syn-rift red bed deposits and the Louann salt deposits in the Eagle Mills Formation poses an important conundrum. Zircon analysis from the Wood River Formation of the South Florida Basin and outcrops of the Dockum Group north of the Ouachita-Marathon orogenic belt indicates deposition ages of approximately 235–195 Ma (Wiley, 2017) and 234–200 Ma (Umbarger, 2018), respectively, leaving a gap between the Louann Salt and the Triassic deposits (Dickinson et al., 2010). Limited exposure of early Mesozoic outcrops south of the Ouachita Mountains and only few drilled wells below the autochthonous Louann Salt in the onshore USA, makes the geological record in the western GoM after the Permian period unclear (Snedden & Galloway, 2019). For example, there is a 90 Myr gap between the Permian strata

and the earliest fully marine Upper Smackover strata formed during the middle Mesozoic drift and cooling phase of the GoM basin in west Texas (Snedden & Galloway, 2019). Seismic surveys conducted along the Yucatán margin and the eastern GoM reveal interpretations of several km thick pre-salt sediments (see section 2.3). Understanding the formation of pre-salt deposits in this area is crucial because, if these deposits are red beds, they can serve as source rocks for stratiform copper deposits that typically form during the early stages of rifting through basin-wide fluid flow systems (Gustafson & Williams, 1981; Hitzman et al., 2005). Evaporites overlying red beds often provide a source of sulphide that is also important for forming sediment-hosted stratiform copper deposits (Sawkins, 1990). Pre-salt strata in the GoM are covered by a thick layer of Louann Salt, and the presence of red beds as copper source rocks may indicate that with optimal thermal and hydrological conditions present may indicate potential for sediment-hosted stratiform copper deposits. Our tectonic subsidence model provides valuable insights necessary to characterize the deposition of these pre-salt strata.

Our model suggests that the onset of Yucatán rotation triggered a sudden increase in tectonic subsidence (Figure 9), creating ample accommodation for sedimentation prior to the marine incursion. The region of high tectonic subsidence shifted further south near the Yucatán margin, implying approximately 4-5 km of tectonic subsidence in the focused stretching zone, and suggesting the presence of a thick pre-salt sedimentary layer. This aligns with the current understanding of a pre-salt sedimentary basin, as mapped by seismic and potential field data (Filina, 2019), indicating continuous deposition. Our model suggests a wider region for pre-salt deposition in the western GoM compared to the eastern parts, with higher tectonic subsidence values near the Yucatán margin, indicating thicker sediment in that area. We propose that the sudden increase in accommodation in the southern GoM, close to Yucatán, facilitated the deposition of sediments from the northern central GoM into the present-day pre-salt sedimentary basin. While the rifting and red bed deposition was continuous until salt deposition, the zone of deformation shifted southward, near the Yucatán margin, which is currently covered by the salt canopy and lacks comprehensive penetrations. As a result, the western paleo drainage and the western branch of the southern paleo drainage actively filled the newly created accommodation by passing previous basin (Figure 10), potentially explaining the larger hiatus between the red beds and the beginning of the Louann Salt in the northern GoM.

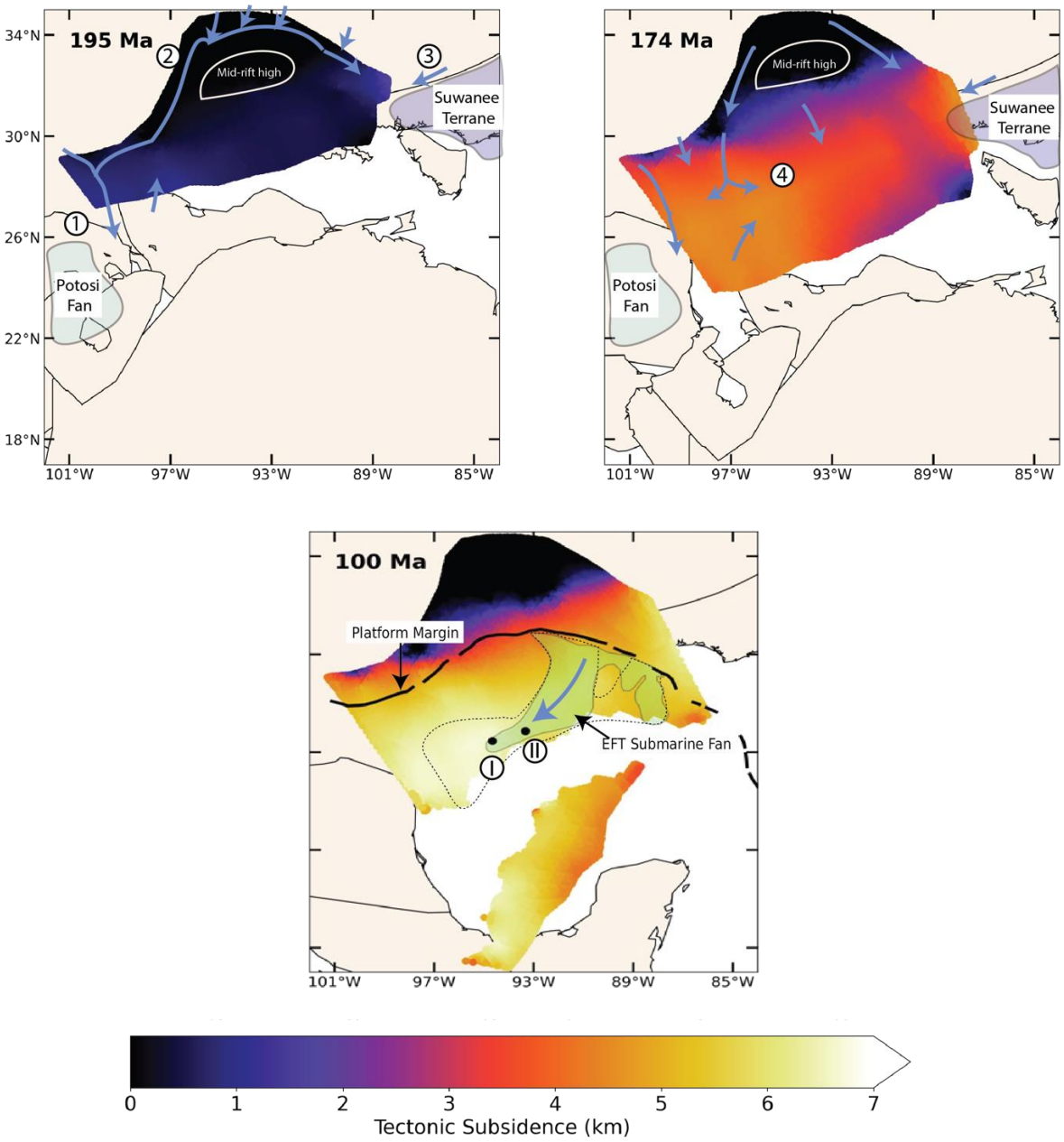

Figure 10. A successor basin fill model showing that a large area in the central GoM may have been filled with red bed sedimentation. Sediment routing was based on an analysis of key wells and their detrital zircon geochronology, which reveals the direction of sediment routing trends (Snedden & Galloway, 2019). 1) The western paleo drainage systems 2) The southern paleo drainage systems have bifurcated around midrift high into two branches: eastern and western branches. 3) The eastern paleo drainage systems. Our model shows tectonic subsidence along these paleo drainages (Right). Our model shows development in rapid tectonic subsidence in a focused region (4). Proposed model and sediment routing for pre-salts deposition based on our tectonic subsidence calculation (left).

This region is wider in the western part of GoM; however, it gets narrower as we move toward the east. We propose that the sedimentation was a continuous process in GoM. However, due to the creation of accommodation during rapid subsidence, the red bed deposition shifted further south near the Yucatán margin. Moreover, western paleo drainage, as well as the western branch of southern paleo drainage, would have been a major source of these sediments. Cenomanian-Turonian (Ceno-Turonian) EFT submarine fans, originating from the southern Louisiana platform margin and extending towards the Tiber (II) and BAHA II (I) well locations in the western GoM (Snedden et al., 2016). Well data is limited further west in the deepwater of the GoM. However, our model suggests that these submarine fans may have extended even farther west, beyond the range of current well penetration, due to increasing differential subsidence towards the west.

5.3 Evolution of Rifting

The accurate determination of the crustal nature in the GoM has been challenging due to the lack of wells penetrating basement. However, recent seismic reflection data from the northern and western Yucatán and northern GoM reveal evidence of magmatism (see section 2.4; Figure 2). The presence of high-amplitude magnetic anomalies coinciding with the SDRs further supports this history of magmatism. Additional geophysical observations, such as the presence of high-velocity crustal intrusions in the lower crust, lend further support to the magma-rich hypothesis (Filina et al., 2022; Steier & Mann, 2019). Velocity models derived from refraction data over distinct high FMAs indicate a high-velocity lower crust in the same region as the interpreted SDRs (Eddy et al., 2014). The inboard Apalachicola Basin (Figure 1) harbors a significant syn-rift volcanic fill (Minguez et al., 2020). Although intriguingly, these features are not positioned at the transition to the oceanic crust (Figure 2). Another common observation in magma-rich margins is the presence of SDRs and lower crustal intrusions, resulting in an abnormally thick crust, presumably formed through subaerial accretion, transitioning into classic submarine oceanic crust which are ~ 7 km thick (Funck et al., 2017; Kelemen & Holbrook, 1995). However, the GUMBO4 line exhibits a relatively thin (~5 km) and uniform oceanic crust, which indirectly supports a magma-poor interpretation (Eddy et al., 2014). The presence of ridge-like basement highs in seismic reflection (Pindell et al., 2014) further supports the magma-poor hypothesis. The examination of aeromagnetic data also reveals compelling indications pointing towards the presence of serpentinised mantle that has been exhumed along the northern margin of the GoM (Minguez et al., 2020; Pindell et al., 2016). Additionally, recent seismic reflection profiles serve as further evidence, illustrating the existence of distinct segments featuring exhumed mantle, alongside occurrences of magmatic intrusion or extrusion along the margins of the Yucatán region (Izquierdo-Llavall et al., 2022). Consequently, an ongoing debate persists regarding whether the GoM can be classified as magma-rich or magma-poor.

The extent of magmatism during the rifting stage is influenced by several factors, including mantle temperature, extension rates, mantle composition, preceding rift history, and the presence or absence of hot active upwelling of the asthenosphere (Armitage et al., 2010; Tetreault & Buiter, 2018; Tugend et al., 2020; White & McKenzie, 1989). Among these factors, mantle temperature is considered the most crucial, as it governs the onset of decompression melting (Tugend et al., 2020). Elevated mantle temperatures increase magma supply, resulting in higher volumes of magmatism in magma-rich margins (White & McKenzie, 1989). The rate of lithospheric extension during breakup is another critical factor that significantly influences

magma supply (Armitage et al., 2010). Magma-rich margins tend to form under conditions where plate separation occurs at a faster pace than in magma-poor margins (Lundin et al., 2014). Mantle composition also plays a role in the volume of melt production with more primitive and volatile-rich mantles generating greater amounts of melt (Cannat et al., 2008). Therefore, the level of magmatism observed at the rift margin and within the GoM is dependent on the complex interaction of these parameters. Our reconstructions provide valuable insights into the temporal and lateral variations in magmatism throughout the evolution of the GoM. Based on the stretching factor, crustal thickness, and extension rate evolution derived from our model, we propose a two-phase development of the GoM's crustal architecture.

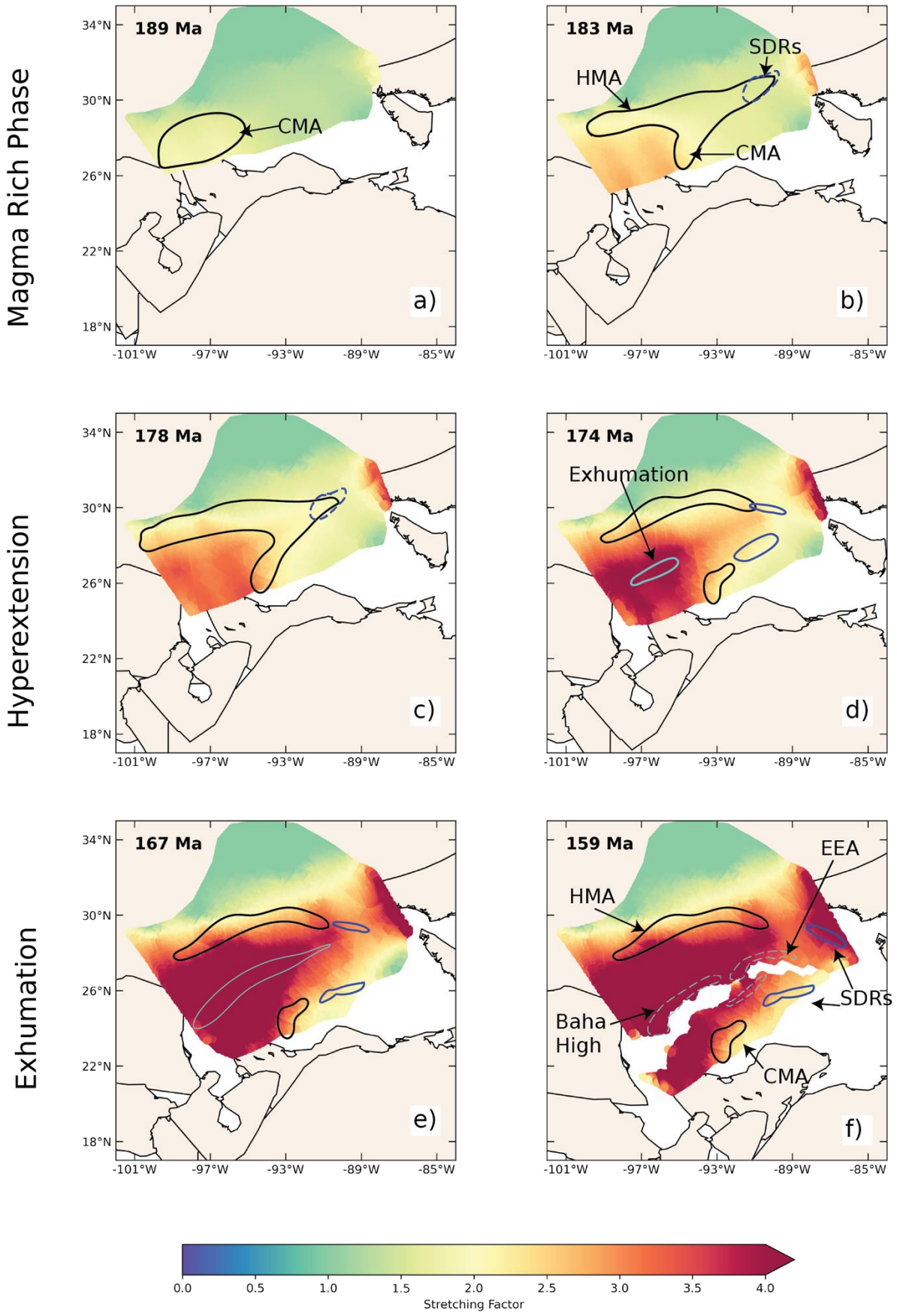
Magma Rich Phase
Hyperextension
Exhumation
189 Ma
CMA
a)
183 Ma
SDRs
HMA
CMA
b)
178 Ma
c)
174 Ma
Exhumation
d)
167 Ma
e)
159 Ma
EEA
HMA
SDRs
Baha
High
CMA
f)
34°N
30°N
26°N
22°N
18°N
-101°W
-97°W
-93°W
-89°W
-85°W
0.0
0.5
1.0
1.5
2.0
2.5
3.0
3.5
4.0
Stretching Factor

1027

Figure 11. a) Formation of CMA aligns well with crustal thinning suggesting rift-related volcanism b) Formation of HMA, LMA, and SDRs. c) Hyperextension started in western GoM. d) Hyperextension propagated to eastern GoM and separation of CMA and HMA. Note HMA, CMA, and SDR have undergone deformation owing to the motion of Florida and Yucatán block motion. Exhumation might have started in western GoM, leading to the formation of BAHA high. e) Seafloor spreading starts. Exhumation in eastern GoM resulting in EEA. f) SDR undergoing deformation owing to the motion of Florida Block. Symmetric and Conjugate EEA separated in central GoM. However, further west, the EEA is asymmetric and tapers out. Magnetic anomalies and SDRs are in black and blue, respectively. The solid light blue color polygon represents the location of possible exhumation. Dashed light blue polygons represented reconstructed BAHA high and EEA anomalies, respectively. Polygons in beige color are rigid continent block.

5.3.1 Magmatism

The transition from rifting to seafloor spreading in passive rift margins occurs when the stretching factor exceeds a certain threshold (Le Pichon & Sibuet, 1981). Volcanic activity is more likely to occur in passive rift margins when the stretching factor exceeds approximately 2 (Le Pichon & Sibuet, 1981). Our model reveals a link between crustal thinning and the formation of the HMA, CMA, and LMA in the western GoM, as well as the positioning of SDRs in the eastern GoM. The CMA in the western GoM formed near the Yucatán margin during the Sinemurian period. As deformation progressed, the region stretched, leading to the formation of the HMA (Figure 11b). Deep seismic data suggest that the FMA and CMA are likely associated with volcanic flows within the syn-rift sections of rift basins (Mickus et al., 2009). The occurrence of the HMA in the western GoM during the Sinemurian period may also be linked to magmatic activity, similar to the CMA. In the eastern GoM, the SDRs observed off the Yucatán margin coincide with the YMA (Steier and Mann, 2019; Filina and Hartford, 2021; Filina and Beutel, 2021). The refraction velocity model (Eddy et al., 2014) indicates that the same region where the SDRs were interpreted in the FMA exhibits a high-velocity lower crust and a Moho associated with intrusions. Liu et al. (2019) have modelled SDRs reflections with high magnetic susceptibilities and densities, which fit well with the potential field data.

One possible explanation for the formation of these SDRs and magnetic anomalies is their proximity to the CAMP event in eastern North America. The elevated subcontinental mantle temperature during the CAMP event would have led to increased decompressional melt generation, resulting in magmatism and lower crustal intrusions (Figure 12). However, the extent of this magmatism would have been limited due to the relatively short duration of the CAMP event. A similar process has been proposed to explain rifting in the northwest Indian Ocean, where the presence of the Deccan Traps, located 1000 km away from the rift zone, created a thermal anomaly that triggered igneous intrusion along the Gopi Rift (Armitage et al., 2010). However, this thermal anomaly was eventually depleted, leading to the formation of a magma-poor Laxmi Ridge margin (Armitage et al., 2010). The production and emplacement of magma during the formation of the GoM might have varied laterally, which could explain the presence of SDRs along the eastern GoM due to its proximity to the CAMP event. Alternatively, the HMA may also be related to the SDRs, but due to its depth and thick salt cover, it remains challenging to determine the presence of SDR patterns in the seismic sections. Another plausible reason for the reduced occurrence of magmatic SDRs in the western GoM could be hindered melt

extraction caused by the greater lithospheric thickness in that region (Izquierdo-Llavall et al., 2022). Furthermore, our model indicates that due to the motion of the Florida Bahamas and Yucatán blocks, these SDRs would have experienced significant deformation and later became separated from each other as a result of seafloor spreading, resulting in their present-day locations (Figure 11 and 12).

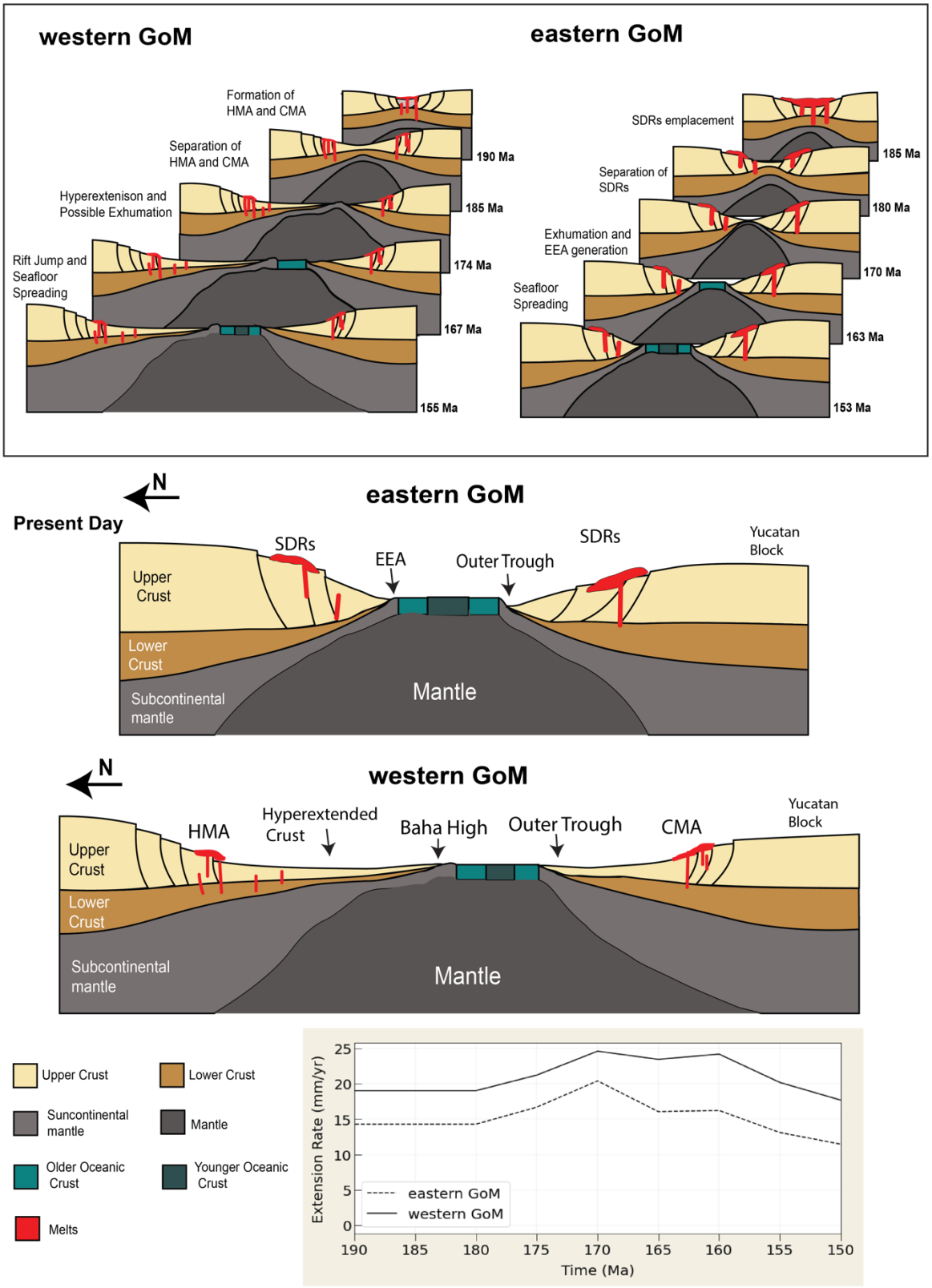

Figure 12. Summary of the evolution of the GoM crustal architecture. Our model suggests that the Mesozoic evolution of the eastern and western GoM basins (roughly along profile GUMBO1

and GUMBO3: Figure 3) commenced as a magma-rich margin. During the Pliensbachian period, there were occurrences of magmatic intrusions and extrusions, resulting in the formation of the HMA, CMA, and LMA in the western GoM, as well as the SDRs in the eastern GoM. The elevated subcontinental mantle temperature during the CAMP event likely caused increased decompressional melt generation, leading to magmatism and lower crustal intrusions. However, this magmatism was short-lived. The subsequent Toarcian development indicates a magma-poor origin characterized by hyperextension and potential mantle exhumation. The rate of extension plays a significant role in shaping the crustal architecture. Higher extension rates (>20 mm/yr) facilitate rapid upwelling of the mantle, resulting in exhumation. As the extension rate is higher farther from the pole of rotation, the western GoM underwent more thinning and wider hyperextension.

5.3.2 Hyperextension and Exhumation

The phase of magma-rich rifting in the GoM was relatively brief due to the short-lived CAMP event. Following the transition from rift to drift, our results indicate a wider region of thinned crust in the western GoM, indicating hyperextension (Figure 11). However, this region narrows as we move towards the central and eastern GoM. In the Bay of Biscay, Le Pichon and Sibuet (1981) estimated that a $\beta>3.2$ was required for the formation of oceanic crust, and for magma-rich margins, these values are even lower. However, our calculations suggest that if this were the case in the GoM, the formation of oceanic crust would have commenced sooner, and further north than currently predicted based on stretching factors. Our analysis reveals a β value of 4 in the wider western GoM basin during the early Toarcian period, while the eastern GoM exhibits a β value of 1.5, and that too within a narrow zone. However, by the late Aalenian-early Bajocian period, the eastern GoM shows a β value of approximately 4, whereas the western GoM reaches around 5.2. This suggests that the rift propagation occurred from west to east, gradually 'unzipping' this hyperextended crust (Figure 11). The unzipping process was triggered by the anticlockwise rotation of the Yucatán block around the rotation pole located in the Florida Straits.

Notably, the extension rate plays a significant role in shaping the crustal architecture of an extending continental crust and its distance from the rotation pole affects the extension rate (Lundin et al., 2014). Closer to the rotation pole, the linear rate of plate extension is relatively small, resulting in a proximal margin characterised by limited extension, where the brittle-ductile transition remains in the crust and brittle deformation occurs along high-angle faults (Colletta et al., 1988). As we move farther away, deformation progresses into the thinning phase, where the complete embrittlement of the crust, fault penetration, and mantle serpentinisation become likely (Lundin et al., 2014). At an even greater distance from the pole, mantle exhumation is predicted. Eventually, the pole of rotation becomes so distant that the linear half-spreading rate exceeds the critical velocity for melting (Bonatti, 1985; Chu & Gordon, 1998). In the case of the GoM, a similar explanation can be applied to understand the crustal architecture. The interpretation of GUMBO1 by van Avendonk et al. (2015) reveals the thinning and wider hyperextension of the continental crust with an exposed upper mantle in the western GoM, which is situated farther away from the rotation pole (Figure 4). Additionally, analogue rock properties-based modelling of the EEA suggests the presence of a narrower zone of exhumed serpentinised mantle along the eastern GoM (Minguez et al., 2020). Recent seismic reflection profiles also indicate segments of

exhumed mantle (Izquierdo-Llavall et al., 2022). These observations, along with the extension rate derived from our model, suggest that by the end of the Early Jurassic, the western GoM would have experienced a prolonged period of hyperextension followed by mantle exhumation prior to seafloor spreading (Figure 12). Moreover, numerical models have demonstrated that extension rates exceeding 20 mm/yr facilitate rapid upwelling of the mantle, leading to an increase in lower crust temperature, ductile deformation, and a decrease in viscosity (Tetreault & Buiter, 2018). Such high extension rates cause the strain in the mantle to decouple from the crust, creating a pathway for exhumation and generating a counterflow in the mantle.
Although our model cannot account for the uplift due to the mantle exhumation process, extension rate calculations from our model can be useful in understanding the evolution of hyperextension phase. Our extension rate calculations suggest that the western GoM experienced a high extension rate (>20 mm/yr) around the middle Toarcian period (~177 Ma). However, during the same period, the eastern GoM exhibited a lower extension rate (Figure 12). Nevertheless, by the late Aalenian period (~171 Ma), the eastern GoM underwent a high extension rate conducive to exhumation, resulting in the formation of symmetric and conjugate EEA. In the western GoM, the magnetic anomaly pattern and seismic results are less clear, but the presence of BAHA high suggests hyperextension and possible mantle exhumation around the middle to late Toarcian. Furthermore, with a shift in extension rate from high to moderate, a rift jump likely occurred, with a more pronounced effect in the wider western GoM compared to the narrower eastern GoM. For a rift jump to occur, Tetreault & Buiter (2018) proposed that a region must be wide enough for the mantle upwelling to reach a depth where it interacts with the ductile lower crust. The deflection of strain by the ductile crustal layers towards the edge of the rift can then shift the upwelling to the rift's edge, abandoning the original rift (Brune et al., 2017; Naliboff & Buiter, 2015). This scenario may have occurred in the western GoM due to its wider zone of extension, resulting in a rift jump and the final margin structure characterised by one narrow margin (Yucatán) and the other with a wider, more hyperextended crust (north-western GoM). As seafloor spreading initiated in the western GoM, the eastern GoM experienced extension within a narrower zone, which likely prevented complete decoupling of the lower crust, resulting in a more symmetrical exhumation pattern.

5.3.3 Post-Rift Thermal Subsidence

The early Cretaceous period was characterised by seafloor spreading, followed by a gradual cooling of lithosphere that resulted in slower thermal subsidence following the stretching and thinning of the lithosphere (Figure 9). Prior to seafloor spreading, the earliest basin-wide deposits in the GoM basin were the Louann salt (Pindell et al., 2021). Following that, the Oxfordian Norphlet-Smackover Formations (NS) were deposited over the salts, resulting in salt-detached raft blocks in a region outlined by the Florida Escarpment, centred on western DeSoto Canyon and eastern Mississippi Canyon (Snedden & Galloway, 2019). Reconstruction of these blocks indicates a south-west direction of rafting by gravity gliding with NS as pre-kinematic and Haynesville-Buckner (HVB), Cotton Valley-Bossier (CVB), and Cotton Valley-Knowles (CVK) synkinetic units deposited at the same time as seafloor spreading (Pilcher et al., 2014; Snedden & Galloway, 2019). Our model suggests that the increase tectonic subsidence towards the rifting zone, as well as from the east to west (Figure 9) can explain the formation of a seaward paleo-slope allowing gravity gliding of raft blocks in the south-west direction.

Our tectonic subsidence suggests a slow increase in tectonic subsidence in the Middle Cretaceus. However, most this period was dominated by carbonates, resulting in the formation of an extensive platform-margin reef system in the northern GoM, which served as an effective barrier preventing siliciclastic sediment from reaching the deep GoM basin, where there was high tectonic subsidence (Snedden & Galloway, 2019). During the Cenomanian-Turonian period, local tectonics and drainage pattern expansion allowed siliciclastic sediment to reach deeper parts of the basin (Snedden & Galloway, 2019). This is evident from the presence of the Eagle Ford-Tuscaloosa (EFT) sandstones which span from the southern Louisiana platform margin to the deepwater of Keathley Canyon and Alaminos Canyon (Snedden et al., 2016). These fluvial-deltaic deposition systems have been discovered in a number of wells as far west as the BAHA II well and the Tiber well (Figure 10). Mapping of these depositions through deep water well of GoM suggests a possible westward deflection (Snedden et al., 2016). Our model suggests that this westward deflection might be influenced by the differential tectonic subsidence in east to west direction. This indicates that the initial tectonic subsidence generated by rifting can have long-term consequences for depositional systems, altering their orientation long after rifting has ceased. Although there is limited deep well in western GoM but our model suggests EFT submarine fan extends further in western GoM (Figure 10).

Sediments from nearby region accumulated in the GoM over millions of years, significantly deepening the basin (Snedden & Galloway, 2019). The presence of vast Louann deposits and accompanying anhydrites, which were covered by sedimentary rocks, contributed to salt tectonics, making precise estimation of the tectonic subsidence value difficult (Ventress et al., 1989). The later Cretaceous subduction of Hess Rise into western North America also influenced tectonic subsidence by an estimated 2-3 km (Wang et al., 2017). These elements, while significant, have been eliminated from our estimation of tectonic subsidence.

Our model provides a comprehensive understanding of the GoM's evolution, encompassing the rift development and the evolution of GoM crust architecture. Furthermore, it offers insights into tectonic subsidence during the early phase of GoM opening, shedding light on the creation of accommodation for the deposition of red beds and pre-salt sediments before seafloor spreading. Overall, our model presents a novel approach to simulating the evolution of a passive rift margin using deformable plates. in older passive margin basins where optimization with present-day crustal thickness is not feasible, our model's parameters, such as the edge length threshold and strain rate resolution, can be employed. However, the initial crustal thickness and exponential stretching coefficient should be chosen thoughtfully, considering the extent and duration of extension. In scenarios where estimating tectonic subsidence from back-stripped data is challenging due to limited sedimentation during the early phase of rifting, our optimised model, constrained by known back-stripped tectonic subsidence or other geophysical data, becomes a valuable tool.

6 Conclusion

Our research introduces an optimised focused deformable plate reconstruction model for highly accurate reconstruction of the GoM's Mesozoic history. Our results reveal that initial tectonic subsidence occurred in the eastern and western regions of northern GoM during the Late Triassic, indicating the infilling of successor basin along three distinct paleo drainage systems.

Furthermore, our reconstruction model demonstrates that the rapid increase in tectonic subsidence near Yucatán in the southern GoM led to sediment deposition in the present-day basin largely bypassing the previous successor basin. The hiatus between the Triassic Red beds and Bajocian salts in northern GoM can thus be attributed to this southward shift in the depocenter.

Our model supports a hybrid origin for the GoM, characterised by an initial phase of magma-rich margins that transitioned into magma-poor margins, exhibiting temporal variability in magmatism. Magmatism in the GoM occurred during the Sinemurian period, resulting in the formation of SDRs. The HMA, LMA, and CMA coincided with crustal thinning in the western GoM, suggesting a magma-rich origin for this margin. However, our model also indicates prolonged hyperextension prior to seafloor spreading during the Pliensbachian-Toarcian. Through focused deformation, we demonstrate the propagation of rift through the unzipping of hyperextended crust from west to east, explaining the distinct crustal architecture observed in the GoM basin. The stretching factor and extension rate calculations derived from our model suggest that the western GoM exhibits a wider hyperextended crust with potential mantle exhumation, which likely occurred during the middle Toarcian. In contrast, the eastern GoM displays a narrower and more symmetric mantle exhumation during the Late Aalenian-Early Bajocian period. Our model further shows that the westward deflection of the Cenomanian-Turonian sandy submarine fan is a result of increasing differential tectonic subsidence from eastern to western GoM and may extend further west. Our study establishes a robust framework for understanding the complex tectonic history of the GoM and provides valuable insights that lay the groundwork for future research on the evolution of passive rift margins worldwide.

Acknowledgements

This project received support from BHP through the STELLAR industry collaboration. SZ was supported by Australian Research Council grant DE210100084 and MS by DP200100966. pyGPlates and GPlates development is funded by the AuScope National Collaborative Research Infrastructure System (NCRIS) program.

Open Research

The model was created by open source software GPlates (https://www.gplates.org) and python library pyGPlates. All the figures are generated using matplotlib library (https://matplotlib.org/) Reconstruction model files and workflows available from **10.5281/zenodo.10165818**

References

Adams, R. L. (2007). Basement Tectonics and the Origin of the Sabine Uplift. *Houston Geological Society Bulletin*, *49*(9), 19–19.

Anderson, T. H., & Schmidt, V. A. (1983). The evolution of Middle America and the Gulf of Mexico–Caribbean Sea region during Mesozoic time. *Geological Society of America*

Bulletin, *94*(8), 941. https://doi.org/10.1130/0016-7606(1983)94<941:TEOMAA>2.0.CO;2

Armitage, J. J., Collier, J. S., & Minshull, T. A. (2010). The importance of rift history for volcanic margin formation. *Nature*, *465*(7300), 913–917. https://doi.org/10.1038/nature09063

Bonatti, E. (1985). Punctiform initiation of seafloor spreading in the Red Sea during transition from a continental to an oceanic rift. *Nature*, *316*(6023), 33–37. https://doi.org/10.1038/316033a0

Boschman, L. M., van Hinsbergen, D. J. J., Torsvik, T. H., Spakman, W., & Pindell, J. L. (2014). Kinematic reconstruction of the Caribbean region since the Early Jurassic. *Earth-Science Reviews*, *138*, 102–136. https://doi.org/10.1016/j.earscirev.2014.08.007

Bott, M. H. P. (1992). The stress regime associated with continental break-up. *Geological Society, London, Special Publications*, *68*(1), 125–136. https://doi.org/10.1144/GSL.SP.1992.068.01.08

Brune, S., Heine, C., Clift, P. D., & Pérez-Gussinyé, M. (2017). Rifted margin architecture and crustal rheology: Reviewing Iberia-Newfoundland, Central South Atlantic, and South China Sea. *Marine and Petroleum Geology*, *79*, 257–281. https://doi.org/10.1016/j.marpetgeo.2016.10.018

Brune, S., Kolawole, F., Olive, J.-A., Stamps, D. S., Buck, W. R., Buiter, S. J. H., et al. (2023). Geodynamics of continental rift initiation and evolution. *Nature Reviews Earth & Environment*, 1–19. https://doi.org/10.1038/s43017-023-00391-3

Cannat, M., Sauter, D., Bezos, A., Meyzen, C., Humler, E., & Le Rigoleur, M. (2008). Spreading rate, spreading obliquity, and melt supply at the ultraslow spreading Southwest Indian

Ridge. *Geochemistry, Geophysics, Geosystems*, *9*(4). https://doi.org/10.1029/2007GC001676

Chenin, P., Schmalholz, S. M., Manatschal, G., & Karner, G. D. (2018). Necking of the Lithosphere: A Reappraisal of Basic Concepts With Thermo-Mechanical Numerical Modeling. *Journal of Geophysical Research: Solid Earth*, *123*(6), 5279–5299. https://doi.org/10.1029/2017JB014155

Christeson, G. L., Van Avendonk, H. J. A., Norton, I. O., Snedden, J. W., Eddy, D. R., Karner, G. D., & Johnson, C. A. (2014). Deep crustal structure in the eastern Gulf of Mexico. *Journal of Geophysical Research: Solid Earth*, *119*(9), 6782–6801. https://doi.org/10.1002/2014JB011045

Chu, D., & Gordon, R. G. (1998). Current plate motions across the Red Sea. *Geophysical Journal International*, *135*(2), 313–328. https://doi.org/10.1046/j.1365-246X.1998.00658.x

Colletta, B., Le Quellec, P., Letouzey, J., & Moretti, I. (1988). Longitudinal evolution of the Suez rift structure (Egypt). *Tectonophysics*, *153*(1), 221–233. https://doi.org/10.1016/0040-1951(88)90017-0

Davison, I., Anderson, L., & Nuttall, P. (2012). Salt deposition, loading and gravity drainage in the Campos and Santos salt basins. *Geological Society of London Special Publications*, *363*, 159–174. https://doi.org/10.1144/SP363.8

Dickinson, W. R., Gehrels, G. E., & Stern, R. J. (2010). Late Triassic Texas uplift preceding Jurassic opening of the Gulf of Mexico: Evidence from U-Pb ages of detrital zircons. *Geosphere*, *6*(5), 641–662. https://doi.org/10.1130/GES00532.1

1312 Ebinger, C. J., Keir, D., Bastow, I. D., Whaler, K., Hammond, J. O. S., Ayele, A., et al. (2017).
1313 Crustal Structure of Active Deformation Zones in Africa: Implications for Global Crustal
1314 Processes. *Tectonics*, *36*(12), 3298–3332. https://doi.org/10.1002/2017TC004526
1315 Eddy, D. R., Van Avendonk, H. J. A., Christeson, G. L., Norton, I. O., Karner, G. D., Johnson, C.
1316 A., & Snedden, J. W. (2014). Deep crustal structure of the northeastern Gulf of Mexico:
1317 Implications for rift evolution and seafloor spreading. *Journal of Geophysical Research:*
1318 *Solid Earth*, *119*(9), 6802–6822. https://doi.org/10.1002/2014JB011311
1319 Eddy, D. R., Van Avendonk, H. J. A., Christeson, G. L., & Norton, I. O. (2018). Structure and
1320 origin of the rifted margin of the northern Gulf of Mexico. *Geosphere*, *14*(4), 1804–1817.
1321 https://doi.org/10.1130/GES01662.1
1322 Escalona, A., Norton, I. O., Lawver, L. A., & Gahagan, L. (2021). Quantitative Plate Tectonic
1323 Reconstructions of the Caribbean Region from Jurassic to Present. *Memoir 123: South*
1324 *America-Caribbean-Central Atlantic Plate Boundary, 2021*, 239–263.
1325 https://doi.org/10.1306/13692247M1233849
1326 Fiduk, J., Weimer, P., Trudgill, B., & Rowan, M. (1999). The Perdido Fold Belt, Northwestern
1327 Deep Gulf of Mexico, Part 2: Seismic Stratigraphy and Petroleum Systems1. *AAPG*
1328 *Bulletin*, *83*.
1329 Filina, I. (2019). Crustal architecture of the northwestern and central Gulf of Mexico from
1330 integrated geophysical analysis. *Interpretation*, *7*(4), T899–T910.
1331 https://doi.org/10.1190/INT-2018-0258.1
1332 Filina, I., & Beutel, E. (2022). *Geological and Geophysical Constraints Guide New Tectonic*
1333 *Reconstruction of the Gulf of Mexico*. https://doi.org/10.1002/essoar.10511463.1

1334 Filina, I., & Hartford, L. (2021). Subsurface structures along western Yucatan from integrated
1335 geophysical analysis. *Marine and Petroleum Geology*, *127*, 104964.
1336 https://doi.org/10.1016/j.marpetgeo.2021.104964
1337 Filina, I., Austin, J., Doré, T., Johnson, E., Minguez, D., Norton, I., et al. (2022). Opening of the
1338 Gulf of Mexico: What we know, what questions remain, and how we might answer them.
1339 *Tectonophysics*, *822*, 229150. https://doi.org/10.1016/j.tecto.2021.229150
1340 Freeland, G. L., & Dietz, R. S. (1971). Plate Tectonic Evolution of Caribbean–Gulf of Mexico
1341 Region. *Nature*, *232*(5305), 20–23. https://doi.org/10.1038/232020a0
1342 Funck, T., Geissler, W. H., Kimbell, G. S., Gradmann, S., Erlendsson, Ö., McDermott, K., &
1343 Petersen, U. K. (2017). Moho and basement depth in the NE Atlantic Ocean based on
1344 seismic refraction data and receiver functions. *Geological Society, London, Special*
1345 *Publications*, *447*(1), 207–231. https://doi.org/10.1144/SP447.1
1346 Gurnis, M., Yang, T., Cannon, J., Turner, M., Williams, S., Flament, N., & Müller, R. D. (2018).
1347 Global tectonic reconstructions with continuously deforming and evolving rigid plates.
1348 *Computers & Geosciences*, *116*, 32–41. https://doi.org/10.1016/j.cageo.2018.04.007
1349 Gustafson, L. B., & Williams, N. (1981). Sediment-Hosted Stratiform Deposits of Copper, Lead,
1350 and Zinc. In B. J. Skinner (Ed.), *Seventy-Fifth Anniversary Volume* (p. 0). Society of
1351 Economic Geologists. https://doi.org/10.5382/AV75.06
1352 Harry, D. L., Londono, J., & Huerta, A. (2003). Early Paleozoic transform-margin structure
1353 beneath the Mississippi coastal plain, southeast United States. *Geology*, *31*(11), 969–972.
1354 https://doi.org/10.1130/G19787.1
1355 Hitzman, M., Kirkham, R., Broughton, D., Thorson, J., & Selley, D. (2005). The Sediment-
1356 Hosted Stratiform Copper Ore System. In J. W. Hedenquist, J. F. H. Thompson, R. J.

Goldfarb, & J. P. Richards (Eds.), *One Hundredth Anniversary Volume* (p. 0). Society of Economic Geologists. https://doi.org/10.5382/AV100.19

Horn, B. W., Goswami, A., Haire, E., Radovich, B., McGrail, A., & Pindell, J. (2016). Extended Abstract: Regional Interpretation Across the Entire Gulf of Mexico Basin – A New Perspective. T*he Houston Geological Society Bulletin*, *58*(7), 31–33. Retrieved from http://archives.datapages.com/data/HGS/vol58/058007/31_hgs580031.htm

Hosseinpour, M., Müller, D., Williams, S., & Whittaker, J. (2013). Full-fit reconstruction of the Labrador Sea and Baffin Bay. *Solid Earth*, *4*, 461–479. https://doi.org/10.5194/se-4-461-2013

Hudec, M. R., Norton, I. O., Jackson, M. P. A., & Peel, F. J. (2013). Jurassic evolution of the Gulf of Mexico salt basin. *AAPG Bulletin*, *97*(10), 1683–1710. https://doi.org/10.1306/04011312073

Hudec, M. R., Dooley, T. P., Peel, F. J., & Soto, J. I. (2019). Controls on the evolution of passive-margin salt basins: Structure and evolution of the Salina del Bravo region, northeastern Mexico. *GSA Bulletin*, *132*(5–6), 997–1012. https://doi.org/10.1130/B35283.1

Huerta, A. D., & Harry, D. L. (2012). Wilson cycles, tectonic inheritance, and rifting of the North American Gulf of Mexico continental margin. *Geosphere*, *8*(2), 374–385. https://doi.org/10.1130/GES00725.1

Izquierdo-Llavall, E., Ringenbach, J. C., Sapin, F., Rives, T., & Callot, J. P. (2022). Crustal structure and lateral variations in the Gulf of Mexico conjugate margins: From rifting to break-up. *Marine and Petroleum Geology*, *136*, 105484. https://doi.org/10.1016/j.marpetgeo.2021.105484

James, P., Ernesto, M. C., Alejandro, C., & Leopoldo, H. (2016). Aeromagnetic Map Constrains Jurassic-Early Cretaceous Synrift, Break Up, and Rotational Seafloor Spreading History in the Gulf of Mexico. In C. M. Lowery, J. W. Snedden, & N. C. Rosen (Eds.), *Mesozoic of the Gulf Rim and Beyond: New Progress in Science and Exploration of the Gulf of Mexico Basin* (Vol. 35, p. 0). SEPM Society for Sedimentary Geology. https://doi.org/10.5724/gcs.15.35.0123

Jarvis, G. T., & McKenzie, D. P. (1980). Sedimentary basin formation with finite extension rates. *Earth and Planetary Science Letters*, *48*(1), 42–52. https://doi.org/10.1016/0012-821X(80)90168-5

Kaban, M. K., Tesauro, M., Mooney, W. D., & Cloetingh, S. A. P. L. (2014). Density, temperature, and composition of the North American lithosphere—New insights from a joint analysis of seismic, gravity, and mineral physics data: 1. Density structure of the crust and upper mantle. *Geochemistry, Geophysics, Geosystems*, *15*(12), 4781–4807. https://doi.org/10.1002/2014GC005483

Kelemen, P. B., & Holbrook, W. S. (1995). Origin of thick, high-velocity igneous crust along the U.S. East Coast Margin. *Journal of Geophysical Research: Solid Earth*, *100*(B6), 10077–10094. https://doi.org/10.1029/95JB00924

Kneller, E. A., & Johnson, C. A. (2011). Plate Kinematics of the Gulf of Mexico Based on Integrated Observations from the Central and South Atlantic. *Gulf Coast Association of Geological Societies Transactions,* 283–300. Retrieved from http://archives.datapages.com/data/gcags/data/061/061001/283_gcags610283.htm

1400 Le Pichon, X., & Sibuet, J.-C. (1981). Passive margins: A model of formation. *Journal of*
1401 *Geophysical Research: Solid Earth*, *86*(B5), 3708–3720.
1402 https://doi.org/10.1029/JB086iB05p03708
1403 Lundin, E.R., & Doré, A. G. (2017). The Gulf of Mexico and Canada Basin: Genetic Siblings on
1404 Either Side of North America. *GSA Today*, 4–11. https://doi.org/10.1130/GSATG274A.1
1405 Lundin, Erik R., Redfield, T. F., & Péron-Pindivic, G. (2014). Rifted Continental Margins:
1406 Geometric Influence on Crustal Architecture and Melting. In James Pindell, B. Horn, N.
1407 Rosen, P. Weimer, M. Dinkleman, A. Lowrie, et al. (Eds.), *Sedimentary Basins: Origin,*
1408 *Depositional Histories, and Petroleum Systems* (Vol. 33, p. 0). SEPM Society for
1409 Sedimentary Geology. https://doi.org/10.5724/gcs.14.33.0018
1410 Maldonado, R., Weber, B., Ortega-Gutiérrez, F., & Solari, L. A. (2018). High-pressure
1411 metamorphic evolution of eclogite and associated metapelite from the Chuacús complex
1412 (Guatemala Suture Zone): Constraints from phase equilibria modelling coupled with Lu-
1413 Hf and U-Pb geochronology. *Journal of Metamorphic Geology*, *36*(1), 95–124.
1414 https://doi.org/10.1111/jmg.12285
1415 Mark V. Shann, K. V.-R., & Horbury, A. D. (2020). The Sureste Super Basin of southern Mexico.
1416 *AAPG Bulletin*, *104*(12), 2643–2700. https://doi.org/10.1306/09172020081
1417 Marton, G., & Buffler, R. T. (1994). Jurassic Reconstruction of the Gulf of Mexico Basin.
1418 *International Geology Review*, *36*(6), 545–586.
1419 https://doi.org/10.1080/00206819409465475
1420 Marzoli, A., Callegaro, S., Dal Corso, J., Davies, J. H. F. L., Chiaradia, M., Youbi, N., et al.
1421 (2018). The Central Atlantic Magmatic Province (CAMP): A Review. In L. H. Tanner

(Ed.), *The Late Triassic World: Earth in a Time of Transition* (pp. 91–125). Cham: Springer International Publishing. https://doi.org/10.1007/978-3-319-68009-5_4

McKenzie, D. (1978). Some remarks on the development of sedimentary basins. *Earth and Planetary Science Letters*, *40*(1), 25–32. https://doi.org/10.1016/0012-821X(78)90071-7

Meyer, B., Saltus, R., & Chulliat, A. (2017). EMAG2v3: Earth Magnetic Anomaly Grid (2-arc-minute resolution) *NOAA National Centers for Environmental Information*. https://doi.org/10.7289/V5H70CVX. Retrieved July 21, 2023, from https://doi.org/10.7289/V5H70CVX

Michael R. Hudec, & Norton, I. O. (2019). Upper Jurassic structure and evolution of the Yucatán and Campeche subbasins, southern Gulf of Mexico. *AAPG Bulletin*, *103*(5), 1133–1151. https://doi.org/10.1306/11151817405

Milliken, J. V. (1988). *Late Paleozoic and Early Mesozoic geologic evolution of the Arklatex Area* (Master's Thesis). Rice University. https://hdl.handle.net/1911/13309

Minguez, D., Gerald Hensel, E., & Johnson, E. A. E. (2020). A fresh look at Gulf of Mexico tectonics: Testing rotations and breakup mechanisms from the perspective of seismically constrained potential-fields modeling and plate kinematics. *Interpretation*, *8*(4), SS31–SS45. https://doi.org/10.1190/INT-2019-0256.1

Montaron, B., & Tapponnier, P. (2009). *A quantitative model for salt deposition in actively spreading basins*. Search and Discovery Article https://doi.org/10.13140/RG.2.1.4078.8000

Müller, R. D., Seton, M., Zahirovic, S., Williams, S. E., Matthews, K. J., Wright, N. M., et al. (2016). Ocean basin evolution and global-scale plate reorganization events since Pangea breakup. *Annual Review of Earth and Planetary Sciences*, *44*(1), 107–138.

1445 Müller, R. D., Zahirovic, S., Williams, S. E., Cannon, J., Seton, M., Bower, D. J., et al. (2019). A
1446 Global Plate Model Including Lithospheric Deformation Along Major Rifts and Orogens
1447 Since the Triassic. *Tectonics*, *38*(6), 1884–1907. https://doi.org/10.1029/2018TC005462
1448 Naliboff, J., & Buiter, S. J. H. (2015). Rift reactivation and migration during multiphase
1449 extension. *Earth and Planetary Science Letters*, *421*, 58–67.
1450 https://doi.org/10.1016/j.epsl.2015.03.050
1451 Nemčok, M. (Ed.). (2016). Determination of unstretched continental, thinned continental, proto-
1452 oceanic, and oceanic crustal boundaries. In *Rifts and Passive Margins: Structural*
1453 *Architecture, Thermal Regimes, and Petroleum Systems* (pp. 76–96). Cambridge:
1454 Cambridge University Press. https://doi.org/10.1017/CBO9781139198844.004
1455 Nicholas, R. L., & Waddell, D. E. (1989). The Ouachita system in the subsurface of Texas,
1456 Arkansas, and Louisiana. In R. D. Hatcher Jr., W. A. Thomas, & G. W. Viele (Eds.), *The*
1457 *Appalachian-Ouachita Orogen in the United States* (Vol. F-2, p. 0). Geological Society of
1458 America. https://doi.org/10.1130/DNAG-GNA-F2.661
1459 O'Reilly, C., Keay, J., Birch-Hawkins, A., Bate, D., Halliday, J., & TGS. (2017). Regional Play
1460 Types in the Mexican Offshore. *GEO ExPro Magazine*. Retrieved from
1461 https://archives.datapages.com/data/geo-expro-magazine/014/014004/pdfs/36.html
1462 Pilcher, R. S., Murphy, R. T., & McDonough Ciosek, J. (2014). Jurassic raft tectonics in the
1463 northeastern Gulf of Mexico. *Interpretation*, *2*(4), SM39–SM55.
1464 https://doi.org/10.1190/INT-2014-0058.1
1465 Pindell, J., Graham, R., & Horn, B. (2014). Rapid outer marginal collapse at the rift to drift
1466 transition of passive margin evolution, with a Gulf of Mexico case study. *Basin Research*,
1467 *26*(6), 701–725. https://doi.org/10.1111/bre.12059

1468 Pindell, J. L. (1985). Alleghenian reconstruction and subsequent evolution of the Gulf of Mexico,
1469 Bahamas, and Proto-Caribbean. *Tectonics*, *4*(1), 1–39.
1470 https://doi.org/10.1029/TC004i001p00001
1471 Pindell, James, Villagómez, D., Molina-Garza, R., Graham, R., & Weber, B. (2021). A revised
1472 synthesis of the rift and drift history of the Gulf of Mexico and surrounding regions in the
1473 light of improved age dating of the Middle Jurassic salt. *Geological Society, London,*
1474 *Special Publications*, *504*(1), 29–76. https://doi.org/10.1144/SP504-2020-43
1475 Pindell, Jim, & Kennan, L. (2009). Tectonic evolution of the Gulf of Mexico, Caribbean and
1476 northern South America in the mantle reference frame: An update. *Geological Society,*
1477 *London, Special Publications*, *328*, 1–55. https://doi.org/10.1144/SP328.1
1478 Reguzzoni, M., & Sampietro, D. (2015). GEMMA: An Earth crustal model based on GOCE
1479 satellite data. *International Journal of Applied Earth Observation and Geoinformation*,
1480 *35*, 31–43. https://doi.org/10.1016/j.jag.2014.04.002
1481 Rowan, M. G. (2014). Passive-margin salt basins: hyperextension, evaporite deposition, and salt
1482 tectonics. *Basin Research*, *26*(1), 154–182. https://doi.org/10.1111/bre.12043
1483 Rubio-Cisneros, I. I., & Lawton, T. F. (2011). Detrital zircon U-Pb ages of sandstones in
1484 continental red beds at Valle de Huizachal, Tamaulipas, NE Mexico: Record of Early-
1485 Middle Jurassic arc volcanism and transition to crustal extension. *Geosphere*, *7*(1), 159–
1486 170. https://doi.org/10.1130/GES00567.1
1487 Salvador, A. (1991). Origin and development of the Gulf of Mexico basin. In A. Salvador (Ed.),
1488 *The Gulf of Mexico Basin* (Vol. J, p. 0). Geological Society of America.
1489 https://doi.org/10.1130/DNAG-GNA-J.389

1490 Sandwell, D. T., Harper, H., Tozer, B., & Smith, W. H. F. (2021). Gravity field recovery from
1491 geodetic altimeter missions. *Advances in Space Research*, *68*(2), 1059–1072.
1492 https://doi.org/10.1016/j.asr.2019.09.011
1493 Sawkins, F. J. (1990). Metal Deposits and Plate Tectonics — An Attempt at Perspective. In F. J.
1494 Sawkins (Ed.), *Metal Deposits in Relation to Plate Tectonics* (pp. 377–388). Berlin,
1495 Heidelberg: Springer. https://doi.org/10.1007/978-3-662-08681-0_11
1496 Scott, K. R., Hayes, W. E., & Fietz, R. P. (1961). Geology of the Eagle Mills Formation, *11*.
1497 Retrieved from http://archives.datapages.com/data/gcags/data/011/011001/0001.htm
1498 Şengör, A. M. C., & Natal'in, B. A. (2001). Rifts of the world. In R. E. Ernst & K. L. Buchan
1499 (Eds.), *Mantle plumes: their identification through time* (Vol. 352, p. 0). Geological
1500 Society of America. https://doi.org/10.1130/0-8137-2352-3.389
1501 Seton, M., Müller, R. D., Zahirovic, S., Gaina, C., Torsvik, T., Shephard, G., et al. (2012). Global
1502 continental and ocean basin reconstructions since 200Ma. *Earth-Science Reviews*, *113*(3),
1503 212–270. https://doi.org/10.1016/j.earscirev.2012.03.002
1504 Snedden, J., Virdell, J., Whiteaker, T., & Ganey-Curry, P. (2016). A basin-scale perspective on
1505 Cenomanian-Turonian (Cretaceous) depositional systems, greater Gulf of Mexico (USA).
1506 *Interpretation*, *4*, SC1–SC22. https://doi.org/10.1190/INT-2015-0082.1
1507 Snedden, J. W., & Galloway, W. E. (2019). *The Gulf of Mexico Sedimentary Basin: Depositional*
1508 *Evolution and Petroleum Applications*. Cambridge: Cambridge University Press.
1509 https://doi.org/10.1017/9781108292795
1510 Snedden, J. W., Norton, I., Hudec, M., Eljalafi, A., & Peel, F. (2018). Palegeographic
1511 Reconstruction of the Louann Salt Basin in the Gulf of Mexico. Presented at the AAPG
1512 Annual Convention and Exhibition, Salt Lake City, Utah. Retrieved from

https://www.searchanddiscovery.com/abstracts/html/2018/ace2018/abstracts/2855365.html

Steier, A., & Mann, P. (2019). Late Mesozoic gravity sliding and Oxfordian hydrocarbon reservoir potential of the northern Yucatan margin. *Marine and Petroleum Geology*, *103*, 681–701. https://doi.org/10.1016/j.marpetgeo.2019.03.001

Tetreault, J. L., & Buiter, S. J. H. (2018). The influence of extension rate and crustal rheology on the evolution of passive margins from rifting to break-up. *Tectonophysics*, *746*, 155–172. https://doi.org/10.1016/j.tecto.2017.08.029

Tugend, J., Gillard, M., Manatschal, G., Nirrengarten, M., Harkin, C., Epin, M.-E., et al. (2020). Reappraisal of the magma-rich versus magma-poor rifted margin archetypes. *Geological Society, London, Special Publications*, *476*(1), 23–47. https://doi.org/10.1144/SP476.9

Umbarger, K. F. (2018, December 31). *Late Triassic North American Paleodrainage Networks and Sediment Dispersal of the Chinle Formation: A Quantitative Approach Utilizing Detrital Zircons* (Thesis). University of Kansas. Retrieved from https://kuscholarworks.ku.edu/handle/1808/27833

Van Avendonk, H., Christeson, G., Norton, I., & Eddy, D. (2015). Continental rifting and sediment infill in the northwestern Gulf of Mexico. *Geology*, *43*. https://doi.org/10.1130/G36798.1

Warren, J. K. (2006). *Evaporites:Sediments, Resources and Hydrocarbons*. Springer Science & Business Media. https://doi.org/10.1007/3-540-32344-9

White, R., & McKenzie, D. (1989). Magmatism at rift zones: The generation of volcanic continental margins and flood basalts. *Journal of Geophysical Research: Solid Earth*, *94*(B6), 7685–7729. https://doi.org/10.1029/JB094iB06p07685

Wiley, K. S. (2017). Provenance of Syn-rift Clastics in the Eastern Gulf of Mexico: Insight from U-Pb Detrital Zircon Geochronology and Thin Sections. *Graduate Theses, Dissertations, and Problem Reports*. https://doi.org/10.33915/etd.6951

Williams-Rojas, C. T., Reyes-Tovar, E., Miranda-Peralta, L., Reyna-Martinez, G., Cardenas-Alvarado, A., Maldonado-Villalon, R., et al. (2012). Extended Abstract: Hydrocarbon Potential of the Deepwater Portion of the “Salina del Istmo” Province, Southeastern Gulf of Mexico, Mexico. *Gulf Coast Association of Geological Societies Transactions*. 641–644. Retrieved from http://archives.datapages.com/data/gcags/data/062/062001/641_gcags620641.htm